

**GSFC JPSS CMO**  
**December 5, 2011**  
**Released**

**Joint Polar Satellite System (JPSS) Ground Project**  
**Code 474**  
**474-00048**

**Joint Polar Satellite System (JPSS)**  
**VIIRS Sea Surface Temperature**  
**Algorithm Theoretical Basis Document**  
**(ATBD)**

**For Public Release**

The information provided herein does not contain technical data as defined in the International Traffic in Arms Regulations (ITAR) 22 CFC 120.10. This document has been approved For Public Release to the NOAA Comprehensive Large Array-data Stewardship System (CLASS).



National Aeronautics and  
Space Administration

**Goddard Space Flight Center**  
**Greenbelt, Maryland**

This page intentionally left blank.



# **Joint Polar Satellite System (JPSS) VIIRS Sea Surface Temperature Algorithm Theoretical Basis Document (ATBD)**

## **JPSS Electronic Signature Page**

### **Prepared By:**

Neal Baker  
JPSS Data Products and Algorithms, Senior Engineering Advisor  
(Electronic Approvals available online at [https://jpssmis.gsfc.nasa.gov/mainmenu\\_dsp.cfm](https://jpssmis.gsfc.nasa.gov/mainmenu_dsp.cfm))

### **Approved By:**

Heather Kilcoyne  
DPA Manager  
(Electronic Approvals available online at [https://jpssmis.gsfc.nasa.gov/mainmenu\\_dsp.cfm](https://jpssmis.gsfc.nasa.gov/mainmenu_dsp.cfm))

**Goddard Space Flight Center  
Greenbelt, Maryland**

This page intentionally left blank.

## **Preface**

This document is under JPSS Ground AERB configuration control. Once this document is approved, JPSS approved changes are handled in accordance with Class I and Class II change control requirements as described in the JPSS Configuration Management Procedures, and changes to this document shall be made by complete revision.

Any questions should be addressed to:

JPSS Ground Project Configuration Management Office  
NASA/GSFC  
Code 474  
Greenbelt, MD 20771

This page intentionally left blank.

## Change History Log

Revision	Effective Date	Description of Changes (Reference the CCR & CCB/ERB Approve Date)
Original	04/22/2011	<b>474-CCR-11-0063:</b> This version baselines D43311, VIIRS Sea Surface Temperature Algorithm Theoretical Basis Document ATDB (ref Y2386), Rev C, dated 09/10/2010, as a JPSS document, version Rev -. This is the version that was approved for NPP launch. Per NPOESS CDFCB - External, Volume V – Metadata, doc number D34862-05, this has been approved for Public Release into CLASS. This CCR was approved by the JPSS Algorithm ERB on April 22, 2011.



This page intentionally left blank.

Northrop Grumman Space & Mission Systems Corp.  
**Space Technology**  
One Space Park  
Redondo Beach, CA 90278

**NORTHROP GRUMMAN**

**Raytheon**



**Engineering & Manufacturing Development (EMD) Phase  
Acquisition & Operations Contract**

**CAGE NO. 11982**

**VIIRS Sea Surface Temperature Algorithm Theoretical  
Basis Document ATBD (ref Y2386)**

**Document Date: 9/10/2010**

**Document Number: D43311  
Revision: C**

**Point of Contact:** Sid Jackson, Modeling & Simulations

**ELECTRONIC APPROVAL SIGNATURES:**

\_\_\_\_\_  
Merit Shoucri, Modeling and Simulations Lead



Prepared by  
**Northrop Grumman Space Technology**  
One Space Park  
Redondo Beach, CA 90278

Prepared for  
**Department of the Air Force**  
NPOESS Integrated Program Office  
C/O SMC/CIK  
2420 Vela Way, Suite 1467-A8  
Los Angeles AFB, CA 90245-4659

Under  
**Contract No. F04701-02-C-0502**

**COMMERCE DESTINATION CONTROL STATEMENT**

The export of these commodities, technology or software are subject to the U.S. Export Laws and Regulations in accordance with the Export Administration Regulations. Diversion contrary to U.S. law is prohibited.

Northrop Grumman Space & Mission Systems Corp. <b>Space Technology</b> One Space Park Redondo Beach, CA 90278		  	
<b>Revision/Change Record</b>			<b>Document Number</b> D43311
<b>Revision</b>	<b>Document Date</b>	<b>Revision/Change Description</b>	<b>Pages Affected</b>
---	01/17/2007	Initial PCIM Release to bring document into Matrix Accountability. Reference original document number: Y2386 delivered in 2002	All
A	08/08/2007	Revision A Release to bring document into Matrix Accountability. Contains revisions found in v5 r5 of the Raytheon document Y2386 delivered June 2005 as part of VIIRS 1.0.4 drop.	All (format and headers )
B	12/19/2008	Revision B. Updates ATBD to conform with changes in Sea Surface Temperature algorithm adopted by NPOESS to follow heritage algorithm	All
C	9/10/2010	Revision C: Updates ATBD in response to Document Convergence RFA 008 (ECR A-329)	9, 14, 27, 29

### Revision/Change Record

### For Document No. Y2386

<b>Symbol</b>	<b>Document Date</b>	<b>Authorization Date</b>	<b>Revision/Change Description</b>	<b>Pages Affected</b>
	03/2003	Sid Jackson	SPCR ALG00000007 NMD-EMD.03.591.009(assigned)	Title Page, Page i, vii, 1, 20-22, 28-39, 41-56, 64-81
	03/2003	Sid Jackson	SPCR ALG00000021 NMD-EMD.03.591.009(assigned)	Title Page, Page i, ii, xi, 10, 22, 28
	05/2005	Sid Jackson	SPCR ALG00000832 NMD-EMD.03.591.009(assigned)	Title Page, Page i-v, vii, xi, 1, 6, 7, 10, 11, 18-21, 27, 29, 39, 41, 43, 47, 49, 58, 59, 60, 61, 62
	06/2005	Sid Jackson	SPCR ALG00000854 NMD-EMD.03.591.009(assigned)	Title Page, Page i-vii, 1, 11, 20-22, 31, 32, 44, 48, 67, 68

## Page

LIST OF FIGURES .....	iii
LIST OF TABLES .....	v
GLOSSARY OF ACRONYMS.....	vi
ABSTRACT .....	viii
1.0 INTRODUCTION .....	1
1.1 PURPOSE .....	1
1.2 SCOPE .....	1
1.3 VIIRS DOCUMENTS .....	1
1.4 REVISIONS.....	1
2.0 EXPERIMENT OVERVIEW .....	2
2.1 OBJECTIVES OF SEA SURFACE TEMPERATURE RETRIEVALS.....	2
2.2 INSTRUMENT CHARACTERISTICS .....	4
2.3 SST RETRIEVAL STRATEGY .....	6
3.0 ALGORITHM DESCRIPTION.....	8
3.1 PROCESSING OUTLINE.....	8
3.2 ALGORITHM INPUT .....	9
3.2.1 VIIRS Data.....	9
3.2.2 Non-VIIRS Data .....	9
3.3 THEORETICAL DESCRIPTION OF SST RETRIEVAL.....	9
3.3.1 Physics of the Problem.....	9
3.3.2 Mathematical Description of the Algorithm .....	14
3.3.2.1 Daytime algorithm: .....	14
3.3.2.2 Nighttime algorithms: .....	14
3.3.2.3 Stratification of the coefficients for systematic environmental influences .....	14
3.3.3 Algorithm Output.....	15
3.4 ALGORITHM SENSITIVITY STUDIES .....	15
3.4.1 Test Data Sets.....	15
3.4.2 Sources of Retrieval Errors .....	16
3.4.2.1     18	

Noise Equivalent Temperature Difference .....	18
3.4.2.2 Band-to-Band Registration and Modulation Transfer Function .....	18
3.4.2.3 19 Modulation Transfer Function.....	19
3.4.2.4 Combined instrumental effects .....	21
3.4.2.5 Parametric dependences of the SST errors .....	22
3.5 PRACTICAL CONSIDERATIONS .....	26
3.5.1 Numerical Computation Consideration .....	26
3.5.2 Programming and Procedural Considerations .....	27
3.5.3 Configuration of Retrievals .....	27
3.5.4 Quality Assessment and Diagnostics.....	27
3.5.5 Exception Handling .....	29
3.6 ALGORITHM VALIDATION .....	30
3.6.1 Pre-Launch Validation.....	30
3.6.2 Post-Launch Calibration and Validation .....	30
3.7 ALGORITHM DEVELOPMENT SCHEDULE.....	35
4.0 ASSUMPTIONS AND LIMITATIONS .....	36
4.1 SENSOR PERFORMANCE .....	36
4.2 DERIVATION OF BULK SST FROM SKIN SST .....	36
4.3 PHYSICAL SST RETRIEVAL.....	38
5.0 REFERENCES .....	39

## LIST OF FIGURES

	<u>Page</u>
Figure 1. IR radiance at satellite height for five standard atmospheres simulated by MODTRAN. The SST at the base of the atmospheres is given in the key in the figure.....	5
Figure 2. As Figure 1, but showing atmospheric transmittance.....	5
Figure 3. SST high level flowchart: Statistical Method.....	8
Figure 8. Distribution of the satellite zenith angle in the synthetic data set used in predictions of the VIIRS SST retrieval accuracy .....	17
Figure 9. Degradation of the SST precision as a function of imperfections in the Band-to-Band Registration. The misregistration ranges from 0.0 to 0.5 of the pixel area.....	19
Figure 10. Degradation of the VIIRS daytime SST retrievals for different models of the MTF, as a function of the Ground Sampling Distance. These results are from a scene containing the Gulf Stream. ....	20
Figure 11. Components of the instrumental sources of error in the VIIRS M15 band at 10.8 $\mu\text{m}$ . The left hand panel shows the errors as a percentage of the radiance measurement, and the right panel after conversion temperature. ....	22
Figure 12. Schematic flow-diagram of the SST EDR error analysis .....	23
Figure 13. Scatter diagrams of the simulated skin SST retrievals, for the daytime NLSW algorithm at left, and the night-time triple band algorithm at left. The daytime retrievals display increasing scatter at higher SSTs, related to associated with increased atmospheric water vapor concentrations. ....	24
Figure 14. Dependences of the skin SST errors on uncorrelated noise in each of the infrared band, expressed as a percentage of the brightness temperature. The top panel shows the SDR errors for the night-time algorithm (green), daytime algorithm (blue) and the day-and-night combination (pink). The center panels show the SDR errors (day-and-night; pink line) and the total error that includes the contribution of the inherent algorithm error (dark blue). The bottom panels show the total skin SST errors for the day-and-night combination and separately for the retrievals during daytime (blue) and nighttime (green). The left column are the results of the simulations in the nadir section of the swath ( $\theta < 40^\circ$ ) and the right column for the end of swath ( $40^\circ < \theta < 53^\circ$ ). The target accuracy is shown in all panels by the yellow line. ....	25
Figure 15. Radiometers installed on ships for the validation of MODIS skin SSTs. Top: the ISAR mounted above the bridge of the M/V <i>Jingu Maru</i> . Middle: CIRIMS mounted above the bridge of the NOAA S <i>Ronald H. Brown</i> . Bottom: M-AERI mounted on an upper deck of the <i>Explorer of the Seas</i> . ....	31

Figure 16. The measurement geometry of a ship-mounted radiometer taking a skin SST measurement. The reflected sky radiance is corrected using a direct measurement of the sky emission, and an accurate value of the surface reflectance (equal to 1-emissivity). .....32

Figure 17. Distributions of the skin SST measurements made from the M-AERI (top), and the CIRIMS (center; from Jessup and Branch, 2008). Bottom: Skin SST measurements from the ISAR on a trans-Atlantic voyage of the M/V *Jingu Maru* from US east-coast ports to Europe, 10-23 July, 2005. The color bar shows the wide range of skin SSTs measured on a single voyage..33

Figure 18. The distribution of the matchups between the MODIS on Aqua and bulk SST measurements from drifting and moored buoys, for 2003. There are 12,536 matchups with the highest quality flag (QF=0) .....34

Figure 20. Mean annual skin-bulk SST difference (left panel), and the surface wind field at the same time (right panel). From Woods et al., 2008. ....37

## LIST OF TABLES

	<u>Page</u>
Table 1. Channel Characteristics of Satellite-borne IR Radiometers .....	6
Table 2. Sensor Performance for Sea Surface Temperature .....	6
Table 5. Scene Temperature Uncertainty .....	21
Table 7. VIIRS SST EDR Quality Flags.....	27



## GLOSSARY OF ACRONYMS

AOI	Angle of Incidence
AMI	Aerosol Model Index
AOT	Aerosol Optical Thickness
ATBD	Algorithm Theoretical Basis Document
ATSR	Along Track Scanning Radiometer
AVHRR	Advanced Very High Resolution Radiometer
BBR	Band-to-Band Registration
BTMn	VIIRS Emissive Band, where n = 12, 13, 14, 15, or 16
CAIV	Cost As an Independent Variable
DCS	Data Collection System on NPOESS
ECMWF	European Center for Medium-Range Weather Forecast
EDR	Environmental Data Record
EOS	Edge of Scan
GLI	Global Imager
GSD	Ground Sample Distance
HCS	Horizontal Cell Size
IPO	Integrated Program Office
IR	Infrared
LOWTRAN	Low-resolution Transmission Model
LWIR	Longwave Infrared
MCSST	Multi-Channel Regression Method SST
MODIS	Moderate Resolution Imaging Spectroradiometer
MODTRAN	Moderate Resolution Transmission Model
MOSART	Moderate Spectral Atmospheric Radiance and Transmittance
MTF	Modulation Transfer Function
MWIR	Midwave Infrared
NCEP	National Centers for Environment Prediction
NEdT	Noise-Equivalent Temperature Difference
NESDIS	National Environmental Satellite, Data and Information Service
NPOESS	National Polar-orbiting Operational Environmental Satellite System

OCTS	Ocean Color and Temperature Scanner
P <sup>3</sup> I	Pre-Planned Product Improvement
PW	Precipitable Water
RMn	VIIRS Reflective Bands, where n = 5, 7, or 9
RMS	Root Mean Square
RVS	Response Versus Scan Angle
SBRS	Santa Barbara Remote Sensing
SRD	Sensor Requirements Document
SST	Sea Surface Temperature
TIR	Thermal Infrared
TOA	Top of Atmosphere
TRMM	Tropical Rainfall Measuring Mission
VIIRS	Visible/Infrared Imager/Radiometer Suite
VIRS	TRMM Visible Infrared Scanner

## ABSTRACT

This is the Algorithm Theoretical Basis Document (ATBD) for Sea Surface Temperature (SST) retrieval from Infrared (IR) radiance measured by the National Polar-orbiting Operational Environmental Satellite System (NPOESS) Visible/Infrared Imager/Radiometer Suite (VIIRS). SST is an input variable for other VIIRS products such as net heat flux. The SST Unit will produce the VIIRS SST Environmental Data Record (EDR), for both a skin SST (i.e. the temperature at the sea surface) and a bulk SST (at a nominal depth of a meter). The SST EDR contains several Key Performance Parameters (KPP) for the NPOESS Mission.

This document describes the theoretical basis of the SST algorithms, which have been developed by the NPOESS algorithm team. These algorithms are built on heritage atmospheric correction algorithms, which use measurements from two or more IR-bands in atmospheric transmission “windows” to correct for the effects of the intervening atmosphere. The VIIRS heritage sensors are the Advanced Very High Resolution Radiometer (AVHRR) and the Moderate Resolution Imaging Spectroradiometer (MODIS). The VIIRS baseline daytime algorithm is a Non-Linear Split Window formulation using VIIRS Bands M15 ( $\lambda=10.8 \mu\text{m}$ ) and M16 ( $\lambda=12.05 \mu\text{m}$ ). The nighttime algorithm also includes measurements from band M12 ( $\lambda=3.7 \mu\text{m}$ ). The algorithms include corrections for changing atmospheric path length across the VIIRS swath though an explicit satellite zenith angle dependence.

Major constraints for the surface temperature algorithms are instrument band spectral and spatial response functions, instrument Noise-Equivalent Temperature Difference (NE $\Delta$ T) for each band, instrument pre-launch calibration and characterization, and on-orbit calibration. Although at-launch coefficients for the atmospheric correction algorithm will be derived through simulations, experience with MODIS has shown the accuracy of the retrievals, and the success of the mission, will depend on the availability and quality of post-launch surface-based measurements for SST retrieval validation and revisions to the algorithms and coefficients..

## 1.0 INTRODUCTION

### 1.1 PURPOSE

This document describes the theoretical basis of the SST algorithm, for retrieval of the VIIRS SST Environmental Data Record (EDR). Algorithm validation, algorithm sensitivity, constraints, limitations, and assumptions are also discussed.

### 1.2 SCOPE

The SST algorithms described in this document will be used routinely to retrieve both skin and bulk SSTs from VIIRS measurements. P<sup>3</sup>I efforts may result in further enhancements to the current operational algorithms.

The next section provides a brief overview. Descriptions of the algorithm are presented in Section 3, along with discussions of algorithm sensitivity to various physical parameters. Calibration and validation are also discussed in Section 3. Constraints, assumptions, and limitations are identified in Section 4.

### 1.3 VIIRS DOCUMENTS

Reference to VIIRS documents is indicated by a number in italicized brackets, e.g., [*V-1*].

### 1.4 REVISIONS

This is revision B of the document, dated November 2008. This is a major revision of the document and was made in response to a major change in the formulations of the default atmospheric correction algorithms for both daytime and nighttime measurements. The daytime formulation is now based on the corresponding algorithms of the heritage instruments, AVHRR and MODIS, and is a form of the Non-Linear SST (NLSST) algorithm (Walton et al., 1998). This is also the fallback algorithm for night-time measurements. The primary night-time atmospheric correction algorithm makes use of measurements in the mid-infrared atmospheric transmission “window.” Substantial contributions to prior versions of this document, including algorithm development, were made by Yimin Ji, Philip E. Ardanuy, Donglian Sun, Quanhua Liu, and Wenli Yang – and others.

## 2.0 EXPERIMENT OVERVIEW

### 2.1 OBJECTIVES OF SEA SURFACE TEMPERATURE RETRIEVALS

Most of the radiant energy arriving at the earth's surface is absorbed by the upper oceans. Some is released locally to the atmosphere, and some is stored for hours to days to seasons. The transport by the surface currents of heat that is subsequently released elsewhere is a major aspect of the climate system, and the poleward advection of heat in the ocean and atmosphere helps define the global climate system, and the response of the atmosphere to the heat released by the ocean determines some important characteristics of the weather. The sea-surface temperature (SST) is an indicator of the distribution of heat in the upper ocean, its patterns reveal the underlying surface currents, and it is a major determining factor in the exchange of heat, momentum and gases with the atmosphere. The ability of satellite-borne radiometers to provide measurements of SST in a self-consistent and accurate fashion on a global scale has resulted in satellite remote sensing having become one of the most important sources of SST data for a wide variety of applications. Its pivotal role in the weather and climate systems has resulted in skin SST being classified as a Key Performance Parameter (*KPP*) in the NPOESS mission.

The SST is a very variable quantity with a range of values from about  $-1.9^{\circ}\text{C}$  (the freezing point of sea water) to greater than  $30^{\circ}\text{C}$ , with spatial gradients in excess of  $1\text{ K km}^{-1}$  possible at surface frontal outcrops. The magnitude of temporal variations of SST around the seasons is often only several degrees, but similar changes can be experienced in the course of a day (e.g. Minnett, 2003; Gentemann et al., 2003; Stuart-Menteth et al., 2003; Gentemann and Minnett, 2008; Gentemann et al., 2008b). A well-known SST perturbation that influences the global-scale weather patterns is the El Niño, in which the SST over the eastern equatorial Pacific may be 4-5 K higher than in the normal situation. SST is also a good indicator of global warming (Good et al., 2007), and for this application, decadal-length time series have to be constructed (Kilpatrick et al., 2001). The characteristics of the SST fields determine the requirements placed on the design, construction and calibration of the satellite radiometers.

The accuracy of infrared SST determination from satellite depends on how well the effects of the intervening, cloud-free atmosphere are corrected. Water vapor is the main contributor to the atmospheric effect in the infrared, and it is very variable in both space and time. This variability requires that for a correction to be effective it has to be applied on a pixel-by-pixel basis. Other gases are relatively well mixed and less problematic in their correction. The atmospheric correction algorithm is effective only in cloud-free conditions, so an important component of the SST processing algorithm is the confident identification of pixels contaminated by cloud effects. The accuracy has improved significantly since the development of radiometers with two or more atmospheric window channels within MWIR and LWIR transmission windows (e.g., McClain et al., 1983; Kilpatrick et al., 2001). The fundamental basis of multi-channel SST algorithms is the differential water vapor absorption in the various atmospheric window regions of the spectrum (McMillin, 1975). This means the temperature corresponding to the spectral radiance measured at satellite height, the brightness temperature (BT), depends on the state of the atmosphere as well as the relative spectral response functions of the channels in question. The difference between the SST and the BT is often referred to as the temperature deficit. The assumption

underpinning the atmospheric correction algorithms is that the temperature deficit in one channel is functionally related to the difference in BTs in other channels:

$$BT_i - SST = f(BT_j - BT_k)$$

where i, j, k, indicate channels of an infrared radiometer (and i can be the same as j or k). The current satellite multi-channel SST algorithm can permit global SST retrievals on space scales of 8 km with a root mean square error ~0.3 K (Kearns et al., 2000; Barton et al., 1993; Legeckis and Zhu, 1997; May et al., 1998; Kilpatrick et al., 2001). MODIS measurement accuracy requirement for SST is 0.35 K (Brown and Minnett, 1996). The current operational Non-Linear SST (NLSST; Walton et al., 1998; May et al., 1998) and the MODIS SST algorithms are based statistical regression methods. The derivation of such algorithms combines satellite and *in situ* measurements, and they have proven to be successful in producing reliable global SST data sets. The current operational SST retrieval methods are based on measurements in two channels in the atmospheric transmission window in the 10-13  $\mu\text{m}$  interval during the daytime and an additional channel in the 3.5-4.2  $\mu\text{m}$  interval in the nighttime. Some research studies also used water vapor information in the statistical method (e.g., Emery et al., 1994). Although physical retrievals have not been used for operational SST retrieval due to the large computational requirement and possible instability, they are promising methods for improving the retrieval precision.

The radiant energy leaving the ocean surface is emitted by a very thin (<1mm) layer, often referred to as the skin layer, and its temperature is called the skin temperature. At the air-sea interface, the ocean is warmer than the overlying atmospheric layer, and thus heat flows from the ocean to the atmosphere. Close to the interface, the heat flow is by molecular conduction, and this requires a vertical temperature gradient. As a consequence, the skin temperature is cooler than that of the water below by a variable amount, up to ~0.5K (Donlon et al., 2002). The heat flow down the skin-layer gradient also provides the energy for evaporation (the latent heat flux into the atmosphere) and the infrared radiative imbalance between the ocean and the atmosphere. By correcting the effects of the atmosphere, the satellite SST retrieval is therefore more physically related to the skin SST than the bulk temperature below. But for some applications an estimate of the bulk SST, attributable to a depth of a meter or more, is required. This need for a bulk temperature has led to the practice of using *in situ* bulk SSTs measured by ocean buoys in the procedure to derive the coefficients used in the atmospheric correction algorithm (see below) and this results in an estimate of the bulk SST, incorporating a mean skin-bulk SST difference. The variability in the difference between skin and bulk temperatures contributes additional uncertainty to the satellite bulk SST retrieval. The relationship between skin and bulk SSTs has been investigated by a number of scientists (e. g., Schluessel *et al.*, 1990; Donlon et al., 2002). Currently, the AVHRR SST is related to bulk SST, while the (A)ATSRs retrieve the skin SST (Závody et al., 1995). The MODIS SST retrieval is a development of the AVHRR SST algorithm, but is a skin temperature product (Brown and Minnett, 1996).

The (A)ATSR retrieval method is based on a physical approach which uses a line-by-line model to simulate the ATSR Top of Atmosphere (TOA) radiances (Závody et al., 1995) and incorporates skin SSTs with the simulated radiances. This method requires accurate models of the atmospheric radiative transfer and of the instrument characteristics, good knowledge of the

spectroscopy of atmospheric gases, and highly accurate on-board calibration, as well as low sensor noise.

The overall scientific objective of the VIIRS SST retrievals is to provide improved operational measurements of both skin and bulk SST fields by using atmospheric correction algorithms based on statistical methods. The VIIRS SST EDR requires a 0.2 K measurement accuracy and a 0.5 K measurement uncertainty. These requirements exceed prior state-of-the-art operational capabilities. However, these are minimum requirements from an environmental research point of view. For example, a few tenths of a degree increase in global SST in a decade reflects a strong global warming trend (Good et al., 2007). Over the tropical oceans, atmospheric convective activities are sensitive to a small change of SSTs (e.g. Webster et al., 1996; Chen and Houze, 1997).

## 2.2 INSTRUMENT CHARACTERISTICS

The VIIRS MWIR and LWIR bands must be positioned to optimize their use for SST determination. Bands in the LWIR atmospheric transmission window are also located near the maximum intensity in Planck's function at temperatures characteristic of the sea surface. Influences of ozone and other variable atmospheric absorbers are best avoided. There are two suitable regions for LWIR band selection: 8-9  $\mu\text{m}$  and 10-13  $\mu\text{m}$ . Three VIIRS LWIR bands are located in these two regions. Figures 1 and 2 show the radiance at the height of the satellite and the atmospheric transmission for the Thermal IR (TIR) spectrum simulated using the MODTRAN atmospheric radiative transfer code and five standard atmospheres. Bands in the MWIR are located where the atmosphere is transparent and less variable. Figure 2 shows that the 3.4-4.2  $\mu\text{m}$  region is a suitable atmospheric window. Two VIIRS MWIR bands are located in this window. The requirement to produce SSTs consistent with those from heritage sensors is also one of the factors for VIIRS band selection. Table 1 shows the bands used to retrieve SST from measurements of existing infrared satellite radiometers. In earlier versions of this ATBD, we investigated the effects of band location in the MWIR and LWIR windows. Those documents summarize the flowdown of the SRD requirements for the VIIRS SST to the present VIIRS IR band selection.

To meet the VIIRS SST measurement requirements, the sensor must have very low radiometric noise in the IR bands. Knowledge of the characteristics of the infrared bands is very important. The detailed specification of the current version of the sensor design is listed in Table 2.

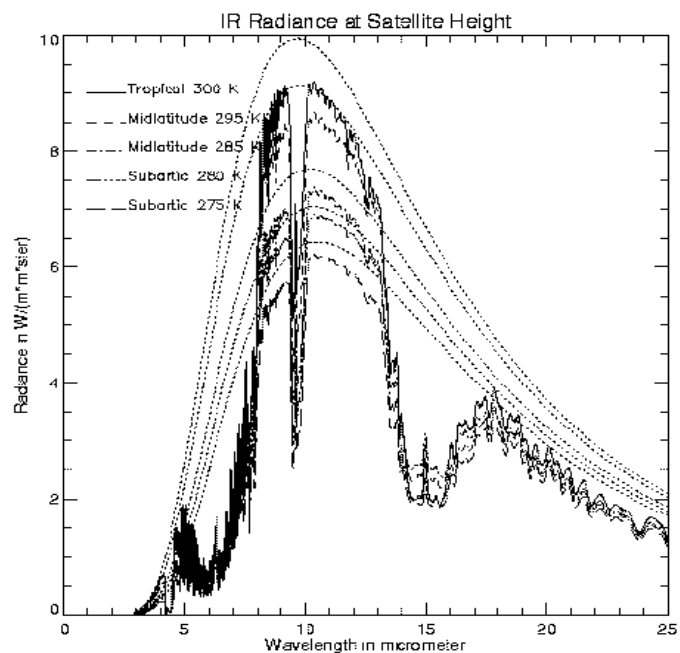


**Figure 1. IR radiance at satellite height for five standard atmospheres simulated by MODTRAN. The SST at the base of the atmospheres is given in the key in the figure.**

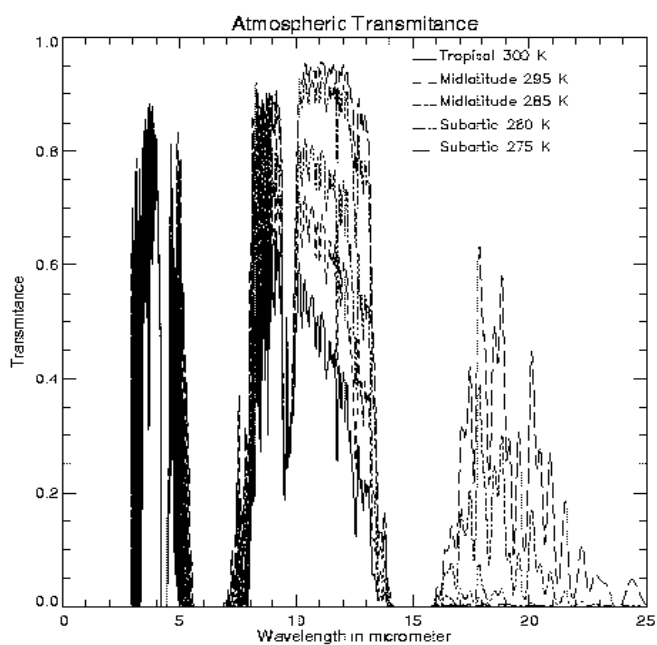


**Figure 2. As Figure 1, but showing atmospheric transmittance.**



**Table 1. Channel Characteristics of Satellite-borne IR Radiometers**

VIIRS baseline		MODIS		AVHRR		(A)ATSR	
$\lambda_{\mu m}$	NE $\Delta$ T K	$\lambda_{\mu m}$	NE $\Delta$ T K	$\lambda_{\mu m}$	NE $\Delta$ T K	$\lambda_{\mu m}$	NE $\Delta$ T K
3.7	0.065	3.75	0.05	3.75	0.12	3.7	0.019
4.0	0.078	3.96	0.07				
		4.02	0.07				
10.8	0.038	11.03	0.05	10.5	0.12	10.8	0.028
12.0	0.070	12.02	0.05	11.5	0.12	12.0	0.025

To meet the VIIRS SST measurement requirements, the sensor must ensure very low radiometric noise for IR bands, especially the 10-12  $\mu m$  window. Well-placed windows in the 3.6-4.2  $\mu m$  are also important. The detailed specification of the current version of the sensor design is listed in Table 2.

**Table 2. Sensor Performance for Sea Surface Temperature**

		Native Sensor						Nadir							
Wave-length μm	Band Width μm	GSD				Ttyp K	NEΔT K	Onboard Aggregation Factor		On ground Aggregation Factor		Effective Algorithm GSD m		Effective Algorithm NEΔT K	
		Nadir m		EOS m											
		Trk	Scn	Trk	Scn			Trk	Scn	Trk	Scn	Trk	Scn		
3.7	0.180	742	262	1094	617	300	0.065	1	3	1	1	742	786	0.038	
4.0	0.155	742	262	1094	617	300	0.078	1	3	1	1	742	786	0.045	
10.8	1.000	742	262	1094	617	300	0.038	1	3	1	1	742	786	0.022	
12.0	0.950	742	262	1094	617	300	0.070	1	3	1	1	742	786	0.040	

## 2.3 SST RETRIEVAL STRATEGY

The following operations are applied to produce the SST:

- A land/ocean mask is used to identify the ocean pixels to process.
- A cloud cover mask and a snow/ice mask are used to eliminate cloud-contaminated or snow/ice-covered pixels. The SST algorithms are not run under confident-cloudy sky conditions; all other cloud conditions the SST is derived, but the results are flagged for quality assurance.
- Satellite zenith angle is read in from the moderate resolution geolocation product.

- A day / night flag based on the solar zenith is to determine whether day or night retrieval is appropriate.
- Calibrated brightness temperatures are read in from the sensor data record (SDR). Appropriate sets of coefficients are loaded for both skin and bulk SST retrievals.
- Skin and bulk SST are both calculated using regression equations from the split window algorithm during the day, and from the triple-window algorithm at night; the nighttime fallback algorithm is the split window formulation.

### 3.0 ALGORITHM DESCRIPTION

#### 3.1 PROCESSING OUTLINE

The atmospheric correction algorithm for SST retrieval is derived using global ancillary data sets and radiative transfer models. The coefficients for the algorithms are obtained through one time simulations and validated using surface observations. Figure 3 depicts the processing concept for SST retrieval.

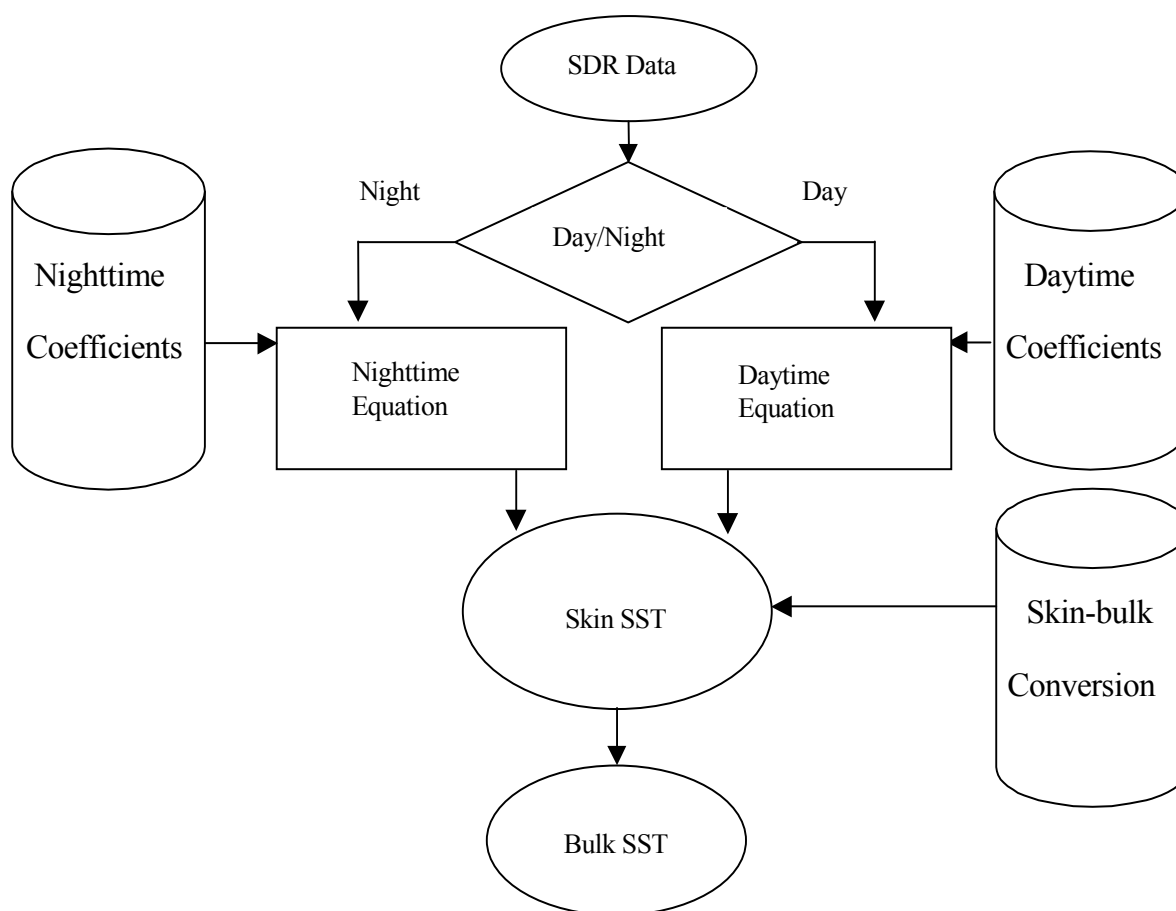


**Figure 3. SST high level flowchart: Statistical Method.**

## 3.2 ALGORITHM INPUT

### 3.2.1 VIIRS Data

Required inputs necessary for the SST retrieval from the VIIRS data stream are cloud mask, snow/ice mask, and TOA brightness temperatures (3.7, 10.76, and 12.05  $\mu\text{m}$ ).

### 3.2.2 Non-VIIRS Data

Non-VIIRS ancillary data includes land/ocean mask.

## 3.3 THEORETICAL DESCRIPTION OF SST RETRIEVAL

### 3.3.1 Physics of the Problem

In clear sky conditions, the outgoing IR spectral radiance at the top of atmosphere can be represented by:

$$L(\lambda, \mu) = \tau(\lambda, \mu)\varepsilon(\lambda, \mu)B(\lambda, T_s) + L_a(\lambda, \mu) + L_s(\lambda, \mu, \mu_0, \varphi_0) + \tau(\lambda, \mu)(1 - \varepsilon(\lambda, \mu))L_d(\lambda, \mu, \mu_0, \varphi_0) + \tau(\lambda, \mu)L_r(\lambda, \mu, \mu_0, \varphi_0) \quad (1)$$

where  $\tau$  is the transmissivity,  $\varepsilon$  the surface spectral emissivity,  $B$  the Planck function,  $L_a$  the upwelling, thermal path radiance,  $L_s$  the path radiance resulting from scattering of solar radiation.  $L_d$  is the solar radiance at the surface and  $L_r$  the solar diffuse radiation and atmospheric thermal radiation reflected by the surface.  $\mu = \cos(\theta)$ ,  $\mu_0 = \cos(\psi)$ , where  $\theta$  is the satellite zenith angle,  $\psi$  the solar zenith angle.  $\varphi_0$  is the azimuth angle between the sun and the satellite.

$\lambda$  is the center wavelength of a narrow spectral interval, defined by the relative spectral response function for each band and detector. Equation 1 is applicable in the 3-14  $\mu\text{m}$  range. The complete simulation of atmospheric radiative transfer is necessary to determine the values of all terms on the right side. This equation has been used in many atmospheric radiation models including LOWTRAN (Kneizys et al., 1988), MODTRAN (Berk et al., 1989), RADGEN (Závody et al., 1995) and MOSART (Cornette et al., 1994). The inversion of Equation 1 is not straightforward if the atmospheric conditions are unknown.

To facilitate the accurate derivation of SST, we should use window bands with no or little atmospheric effect on the propagation of the infrared radiation. As shown in Figures 1 and 2 the wavelength intervals between 3.5–4.2  $\mu\text{m}$ , 8–9  $\mu\text{m}$ , and 10–13  $\mu\text{m}$  are atmospheric transmission windows. For a perfect window, the total atmospheric transmittance  $\tau(\lambda, \mu)$  would be 1.0. However, as indicated in Figure 2, the transmittances at these windows are <1.0 and are functions of the atmospheric state. The main absorber for these windows is atmospheric water vapor.

The effect of water vapor in the transmissivity of the different spectral windows is illustrated in Figure 4 (Sobrino et al., 2003). The water vapor effects are much more pronounced in the thermal infrared window, with the mid-infrared transmission window being much less sensitive

to variations in the water vapor. Figure 4 is based on MODTRAN simulations using atmospheric states derived from radiosondes in the TIGR (TOVS Initial Guess Retrieval data base) (Chesters et al., 1983).

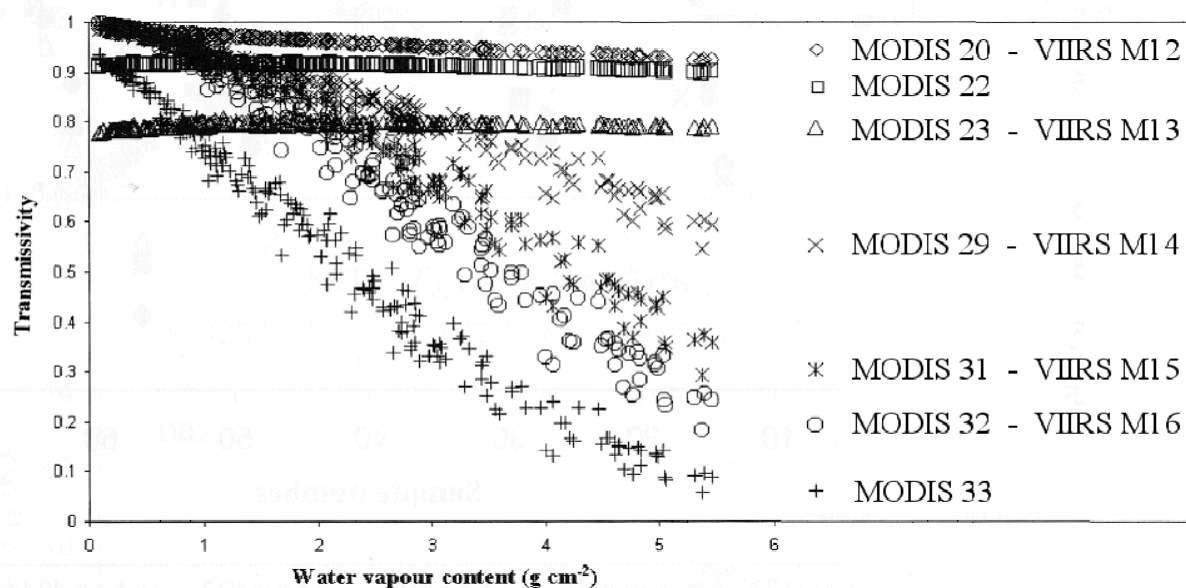


**Figure 4 The relationships between atmospheric transmissivity and atmospheric water vapor content (after Sobrino et al., 2003). The data points were derived by radiative transfer modeling using a large data base of atmospheric profiles and the relative spectral response functions of the MODIS on *Terra*. The MODIS bands, and the corresponding VIIRS bands, are shown in the key at the right.**

The saturation water vapor concentration is governed by the Clausius-Clapeyron equation which indicates that the saturation vapor pressure of a gas varies approximately exponentially with absolute temperature. Given the close thermodynamic coupling between the ocean and atmosphere, it is expected that a clear relationship exists between the atmospheric water vapor content and the SST. This has been demonstrated with satellite microwave radiometric measurements (e.g. Stephens, 1990) which reveal a non-linear increase in integrated water vapor content (precipitable water) with SST (Figure 5).

The consequence of the relationships between SST and atmospheric water vapor, and between water vapor and spectrally dependent atmospheric transmissivity, lead to a non-linear dependence of the brightness temperatures, measured at orbital height in the different spectral bands of infrared radiometers, on the SST. This is illustrated in Figure 6 which shows simulated brightness temperature deficits (the difference in the brightness temperature and the SST) in selected MODIS bands that correspond to VIIRS bands, as functions of SST. The use of MODIS relative spectral response functions in these simulations in place of those from VIIRS will introduce small discrepancies, but serve to illustrate the nature of the interaction between the cloud-free atmosphere and the infrared radiation.

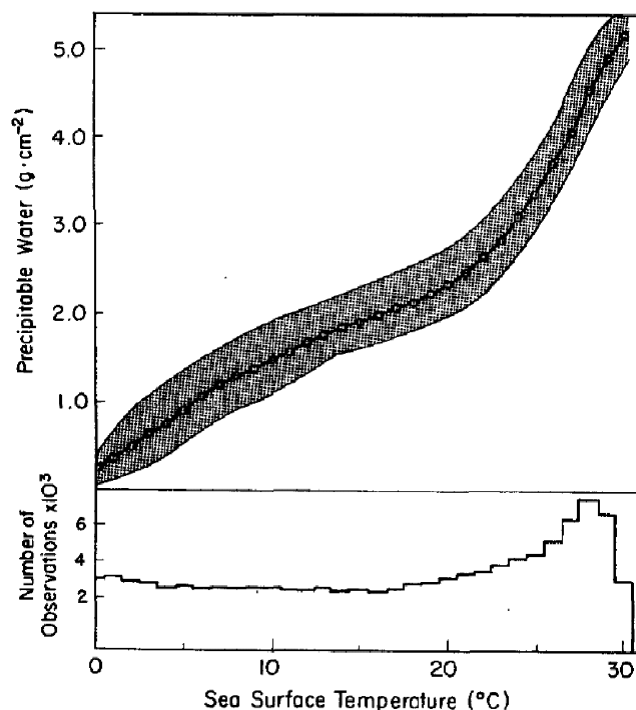


**Figure 5 The relationship between annually averaged vertically integrated atmospheric water vapor content (precipitable water) and the SST (top), and the histogram, of the global SST values (bottom). The data were derived from measurements of the Scanning Multichannel Microwave Radiometer (SMMR) on the Nimbus-7 satellite. (From Stephens, 1990)**

The representation of the cloud-free atmospheric variability for the radiative transfer code was provided by a set of atmospheric profiles, 2790 in number, from a data assimilation model used in weather prediction. These were derived from the output of the ECMWF (European Centre for Medium-range Weather Forecasting) data assimilation model at  $10^\circ$  latitude-longitude resolution over the oceans for 12 realizations through 1996. This has the advantage of near-uniform coverage over the oceans and good sampling in time.

The atmospheric radiative transfer model used to derive the results shown in Figure 6 is the line-by-line spectral code developed for the algorithm derivation for the ATSR (Závody et al., 1995), adapted to accommodate the latest version of the water-vapor continuum spectrum (Clough et al., 1989, subsequently revised by Han et al., 1997 and discussed in Merchant et al., 1999), with improved spectral parameters for atmospheric components from the AFGL data base. This radiative transfer model is also the basis of the atmospheric correction algorithm applied to the measurements of the Along Track Scanning Radiometer (ATSR) series on the European satellites ERS-1, ERS-2 and Envisat. Again, the SST retrievals have been validated using independent measurements (Mutlow et al., 1994; Smith et al., 1994; Noyes et al., 2006). For the MODIS simulations, the model spectral ranges were 3.5 to  $4.2\mu\text{m}$  and 6.2 to  $14.7\mu\text{m}$ , with a spectral resolution of  $0.04\text{ cm}^{-1}$ .

The output of the radiative transfer model comprises three sets of spectra for each atmospheric profile. These are of the upwelling atmospheric emission at the top of the atmosphere ( $L_{\text{atm}\uparrow}(\theta, \lambda)$ ), downwelling atmospheric emission at the bottom of the atmosphere ( $L_{\text{atm}\downarrow}(\theta, \lambda)$ ), and of the atmospheric transmission ( $\tau(\theta, \lambda)$ ), where  $\theta$  is the propagation angle relative to vertical. The spectrum of the total infrared radiance at the top of the atmosphere ( $L_{\uparrow}(\theta, \lambda)$ ) is derived by:

$$L_{\uparrow}(\theta, \lambda) = L_{\text{atm}\uparrow}(\theta, \lambda) + ((1 - \epsilon(\theta, \lambda)) * L_{\text{atm}\downarrow}(\theta, \lambda) + \epsilon(\theta, \lambda) * B(\text{skinSST}, \lambda)) * \tau(\theta, \lambda) \quad (2)$$

where  $\epsilon(\theta, \lambda)$  is the emissivity of the sea-surface at wavelength  $\lambda$  and emission angle  $\theta$ , and  $B$  is Planck's function at the temperature of the skin of the ocean, determined for each profile as an imposed air-sea temperature difference. The propagation of the infrared radiation through the atmosphere can be considered as a collimated beam at a given zenith angle because at infrared wavelengths the atmosphere can be considered to be non-scattering. The emission angle equals the satellite zenith angle.

The surface emissivity enters in two places: in the emission of the sea surface and in the reflection of  $L_{\text{atm}\downarrow}(\theta, \lambda)$  as, through Kirchhoff's Law, the reflectivity is  $(1 - \epsilon(\theta, \lambda))$ . The values used in these simulations were taken from the modeled results of Watts et al., 1996) which includes a specific wind-speed dependence. Subsequent research has shown that the wind speed dependence of  $\epsilon(\theta, \lambda)$  has been over-emphasized in a number of well-used models results (e.g. Masuda et al., 1988, and Wu and Smith, 1997) as well as Watts et al., 1996) when compared to hyperspectral measurements at sea (Hanafin and Minnett, 2005; Nalli et al., 2008a) and more rigorous modeling (Nalli et al., 2008b). Thus, the consequences of the use of a single emissivity, neglecting wind speed effects, for each emission angle are of little consequence in these simulations.

Simulations were done for a range of satellite zenith angles ( $\theta$ ) and air-sea temperature differences (i.e. a skin SST was specified at the base of each atmosphere through a range of air-sea temperature differences: -3, -2, -1, 0 1 K). The behavior of the temperature deficits in *Terra* MODIS Bands 20, 23, 31 and 32 are shown in Figure 6. Figure 6a is for a satellite zenith angle of  $0^\circ$  (i.e. at nadir, at the sub-satellite track at the center of the swath) and Figure 6b at a satellite zenith angle of  $55^\circ$ , towards the edges of the swath. The points in each scatter diagram occur in groups of five representing the five different air-sea temperature differences at the base of each representation of the atmosphere. The magnitudes of the temperature deficits increase with satellite zenith angle, resulting from the effects of the increased atmospheric path length and decreasing surface emissivity. For bands 31 and 32 in the thermal infrared there are two distinct regimes with different sensitivities of the temperature deficits to the SST. This is caused primarily by the increasing atmospheric water vapor burden, which is highly correlated with the SST (Stephens, 1990), and which contributes a larger proportion of the spectral radiance measured in space in tropical conditions (Figure 5) than in higher latitudes.

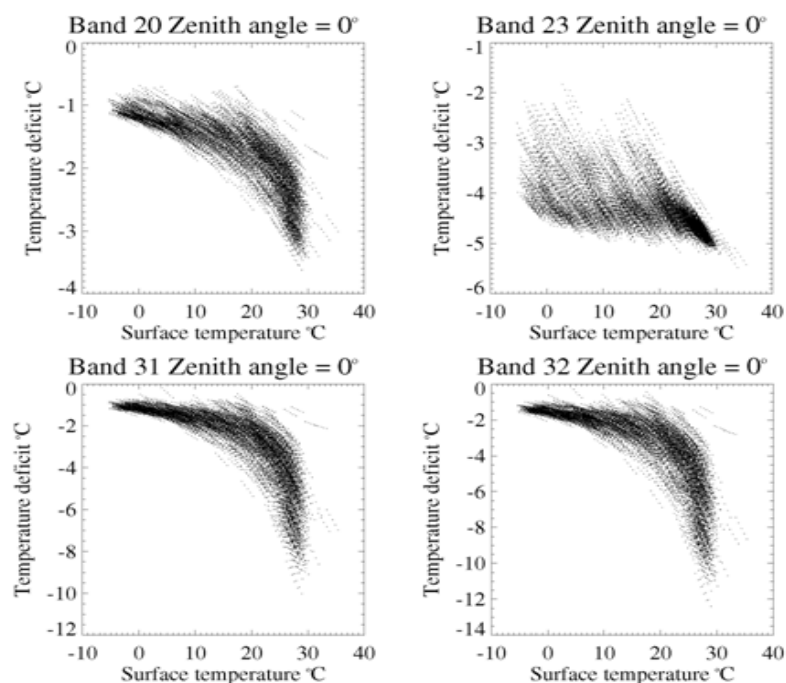


**Figure 6 Simulated brightness temperature deficit for the MODIS bands corresponding to the VIIRS bands to be used for SST derivation. These simulations are expected to approximate very well the characteristics of the VIIRS measurements. The values here are for nadir measurement, at the center of the swath, at a zenith angle of 0°.**

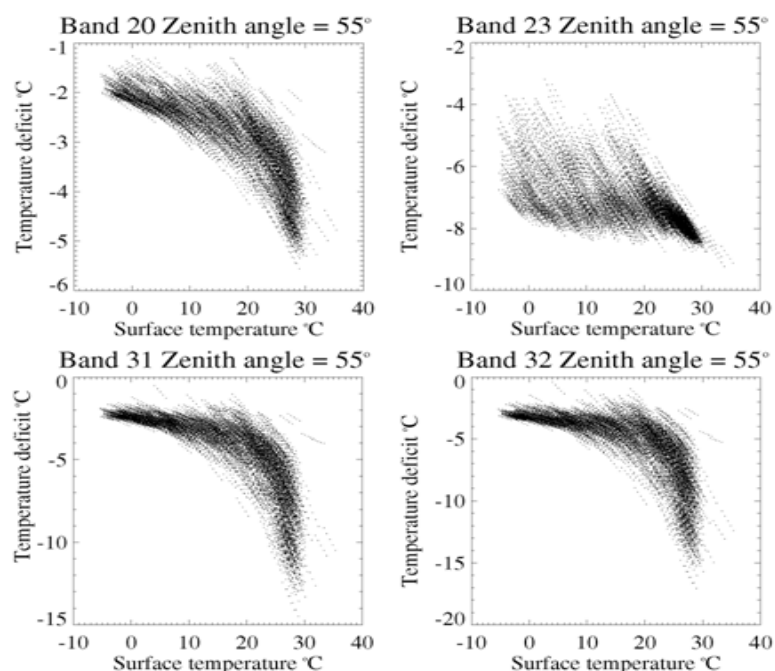


**Figure 7 As Figure 6, but for a satellite zenith angle of 55°.**



### 3.3.2 Mathematical Description of the Algorithm

The baseline VIIRS SST algorithm is based on statistical regression methods. The heritage approach is the nonlinear multi-channel SST (NLSST; Walton, 1988). Such methods require the availability of high quality *in situ* data for both the derivation of the coefficients of the algorithms and for subsequent validation of the SST retrievals.

#### 3.3.2.1 Daytime algorithm:

The NLSST algorithm takes the form:

$$SST = a_0 + a_1 T_{11} + a_2 (T_{11} - T_{12}) RSST + a_3 (T_{11} - T_{12}) (\sec(z) - 1) \quad (3)$$

where  $a_0$ ,  $a_1$ ,  $a_2$ ,  $a_3$  are coefficients derived by regression analysis,  $T_{11}$  is the measured brightness temperature at 11  $\mu\text{m}$  (VIIRS band M15),  $T_{12}$  is the measured brightness temperature at 12  $\mu\text{m}$  (VIIRS band M16), RSST is a modeled, first guess SST, and  $z$  is the sensor zenith angle. RSST is used to scale the coefficient  $a_2$  to account for the varying relationship between the atmospheric water vapor distribution and the surface temperature.

Following the approach of the AVHRR Pathfinder SST project (Kilpatrick et al., 2001), this algorithm is stratified into two regimes by  $T_{11}$ - $T_{12}$  with a switch point at 0.8 K. For the range of 0.6 K to 1.0 K, results from the two stratifications are linearly interpolated..

#### 3.3.2.2 Nighttime algorithms:

The nighttime algorithm takes the form:

$$SST = a_0 + a_1 T_{11} + a_2 (T_{3.7} - T_{12}) RSST + a_3 (\sec(z) - 1) \quad (4)$$

where  $a_0$ ,  $a_1$ ,  $a_2$ ,  $a_3$  are coefficients derived by regression analysis (but are different from those in Equation 12),  $T_{3.7}$  is the measured brightness temperature at 3.7  $\mu\text{m}$  (VIIRS band M12).

The VIIRS baseline algorithm uses equation 3 for daytime retrieval and equation 4 for nighttime retrieval.

#### 3.3.2.3 Stratification of the coefficients for systematic environmental influences

Following the experience with the heritage sensors, the AVHRR Pathfinder SST and the MODIS skin SST, the coefficients of the NLSST atmospheric correction algorithm are derived and applied in two groups defined by a threshold in the brightness temperature differences,  $BT_{11}$ - $BT_{12}$ , i.e. the brightness temperature differences between VIIRS bands M15 and M16. This is a surrogate for the atmospheric water vapor content, and divides the atmospheric conditions into “dry” and “moist.” The “dry” conditions are characterized by small  $BT_{11}$ - $BT_{12}$  and “moist” conditions by larger values. The value of the transition point is 0.8K, and for the interval of  $\pm 0.2\text{K}$  on either side of this the SST will be derived using both sets of coefficients and the final values derived by linear interpolation using the actual  $BT_{11}$ - $BT_{12}$  value.

### 3.3.3 Algorithm Output

SST is retrieved for all pixels that are not flagged as confident cloudy by the VIIRS cloud mask for all satellite viewing angles. Quality flags are provided for each pixel to convey the confidence in the cloud screening. Two VIIRS LWIR bands are used in the VIIRS baseline non-linear split window (NLSW) algorithm. At night a three-band algorithm will be used. Separate sets of algorithm coefficients are used for bulk SST and skin SST.

## 3.4 ALGORITHM SENSITIVITY STUDIES

Clearly, the pre-launch studies of the VIIRS SST retrievals must be conducted on surrogate data. Several data sets have been used to predict the accuracy of the VIIRS skin and bulk SST retrievals. These primarily encapsulate the effects of environmental variability and a separate set of models are used to determine the consequences of instrumental artifacts in the simulated on-orbit measurements

### 3.4.1 Test Data Sets

Two primary data sets have been used to predict the errors in the VIIRS SST algorithms:

- A synthetic set of VIIRS measurements has been derived using atmospheric parameters and surface conditions from NWP models and data products from heritage instruments, extensive atmospheric radiative transfer modeling, with a current VIIRS instrument model and the NPOESS satellite model. This synthetic data set is intended for the study of the behavior of several VIIRS EDRs, not just the SSTs. These synthetic data were derived using end-to-end simulations and are believed to be the most realistic representation of the VIIRS measurements. The derivation of the data set is described in “NPP Operational Algorithm Proxy and Synthetic Test Data Description” (Document D45702, dated 12/20/07).
- The MODIS Match-Up Data Bases are compilations of collocated, coincident measurements of the MODIS brightness temperatures and surface measurements, primarily from drifting and moored buoys, generated for the derivation of the coefficients used in the MODIS atmospheric correction algorithms. There is a data base for each MODIS on *Terra* and *Aqua*. They are also used to determine the characteristics of the residual uncertainties. Included in the data base is are the radiometric skin SSTs derived from ship-board instruments: M-AERI (Minnett et al., 2001), CIRIMS (Jessup and Branch, 2008) and ISAR (Donlon et al., 2008). These radiometers are discussed in more detail below in terms of their roles in validating SST retrievals. The residual instrumental artifacts of MODIS are included, implicitly, in these data.

An additional three data sets, used extensively in the initial studies of the VIIRS SST algorithm as describes in earlier editions of the ATBD, remain available as required to investigate the SST retrieval errors:

- A set of 299 global observations of skin SST with radiosonde atmospheric profiles and coincident satellite passes (Emery et al., 1994) plus 6 standard atmosphere profiles and

surface temperatures. In order to simulate the daytime radiance, 400 simulations were performed for each pixel, in order to employ different satellite viewing angles, solar zenith angles and azimuth angles. There are 121,170 samples. The samples for seven SST categories from 270-275 K to 300-305 K are 240; 1,160; 1,120; 2,200; 2,120; 3,917; and 1,360. Half of the data were randomly picked as training data, others as testing data. Sensor noises are applied to both training and testing data. Absolute radiometric errors (0.4%) were applied only to testing data.

- A global NCEP snapshot of surface temperature at  $2.5^\circ \times 2.5^\circ$  resolution supplied by NCEP (Kalnay et al., 1996), with matching atmospheric profiles. There are 26,590 samples in the simulation. The samples for seven SST categories from 270-275 K to 300-305 K are 100, 343, 405, 310, 318, 910, and 265.
- A set of 1.3 km resolution surface temperature scenes derived from AVHRR 1b data.

The characteristics of the VIIRS synthetic data sets, as relevant to the SST retrievals, are summarized as histograms in Figure 7. The distribution of satellite zenith angle ( $\theta$ ) in the synthetic data set is shown in Figure 8

### 3.4.2 Sources of Retrieval Errors

The sources of error in accuracy and precision in the VIIRS SSTs fall into two categories: those that are associated with imperfections in the instrument, and those that arise from imperfections in the atmospheric correction algorithm. The instrumental effects include:

- The inherent noise in the detectors, the Noise Equivalent Temperature Difference (NE $\Delta$ T)
- Band-to-band registration (BBR)
- Modulation Transfer Function (MTF)
- Calibration errors, such as imperfections in the knowledge of the emissivity and surface temperature of the on-board black body target, and of stray radiation falling on the detectors.

The instrumental errors will be better understood and quantified after the system-level thermal vacuum pre-launch testing of the VIIRS Flight Units. The errors in the atmospheric correction result from the use of a very simple algorithm to approximate a very complex set of physical processes that govern the radiative transfer of the infrared radiation from the sea surface to the aperture of the instrument at satellite height.

The instrumental sources of error have been examined using the synthetic VIIRS data, by comparison of VIIRS instrument characteristics with those of the heritage AVHRR and MODIS instruments, and examining the errors inherent in the atmospheric correction using the MODIS Match-Up Data Bases.

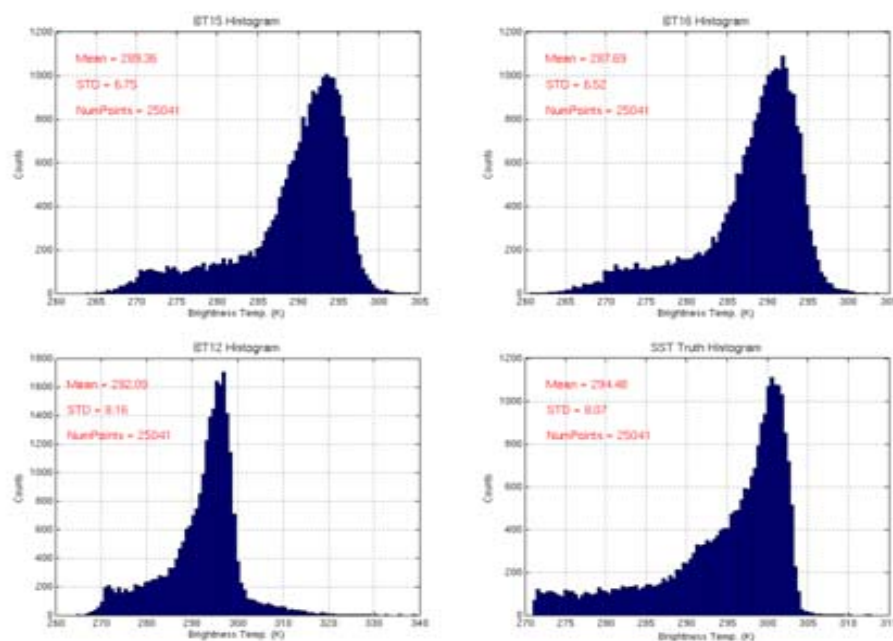


**Figure 8** Histograms of simulated top-of-atmosphere brightness temperatures measured in VIIRS Bands M15 ( $\lambda = 10.8 \mu\text{m}$ ), M16 ( $\lambda = 12.0 \mu\text{m}$ ) - top row - and M12 ( $\lambda = 3.7 \mu\text{m}$ ) - bottom left. The distribution of SSTs in the synthetic data set is shown at bottom right.

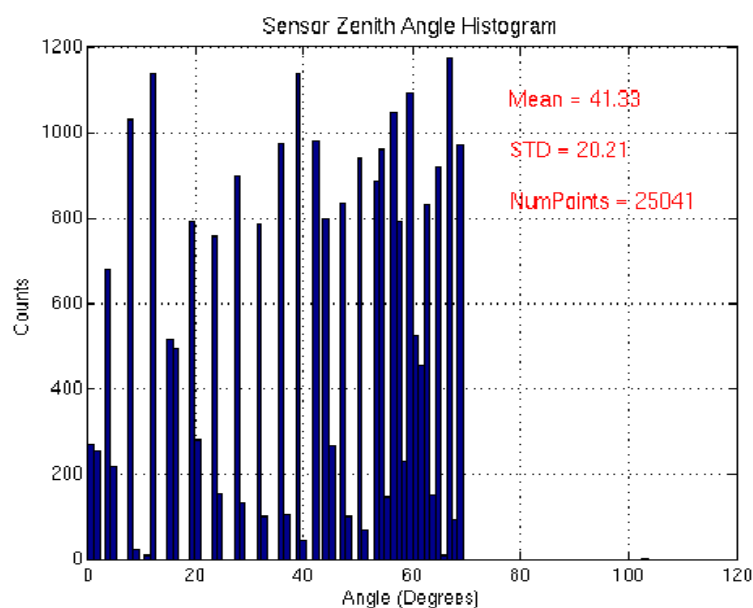


**Figure 8.** Distribution of the satellite zenith angle in the synthetic data set used in predictions of the VIIRS SST retrieval accuracy

### 3.4.2.1 Noise Equivalent Temperature Difference

Table 3 shows the specified Noise Equivalent Temperature Differences (NE $\Delta$ Ts) for the VIIRS bands used in the SST retrieval, together with the values determined in the pre-launch calibration and characterization of the Engineering Design Unit in thermal-vacuum testing. The ratio of the measured to specified NE $\Delta$ T provides a significant margin. Note that the pixel-aggregation along the scan lines results in the averaging of three pixels for the satellite zenith angle ( $\theta$ )  $< 31.59^\circ$  and, of two pixels for  $31.59^\circ < \theta < 44.82^\circ$ ; in these ranges the NE $\Delta$ Ts are reduced by  $\sqrt{3}$  and  $\sqrt{2}$ .

**Table 3. Specified and measured NE $\Delta$ Ts of the VIIRS infrared bands used in the SST retrieval.**

Band	NE $\Delta$ T [K]	Scene T [K]	NE $\Delta$ T/ T	Condition	Spec NE $\Delta$ T	Ratio to Spec
M12	0.174	270	0.0643%	rad spec	0.396	0.44
M15	0.027	300	0.0091%	rad spec	0.070	0.39
M16	0.038	300	0.0126%	rad spec	0.072	0.53

### 3.4.2.2 Band-to-Band Registration and Modulation Transfer Function

Figure 9 shows the influence of Band-to-Band Registration (BBR) errors on the precision of the skin SST derived with the baseline daytime VIIRS split window algorithm. This is based on a study of AVHRR test scenes. The misregistration has significant impact on the retrieval precision when the measurement noise is small. As the sensor noise increases, the influence of BBR errors becomes less important. Therefore, the BBR is not a critical issue for SST retrieval, especially where the SST gradients are small.

### Split Window SST Precision

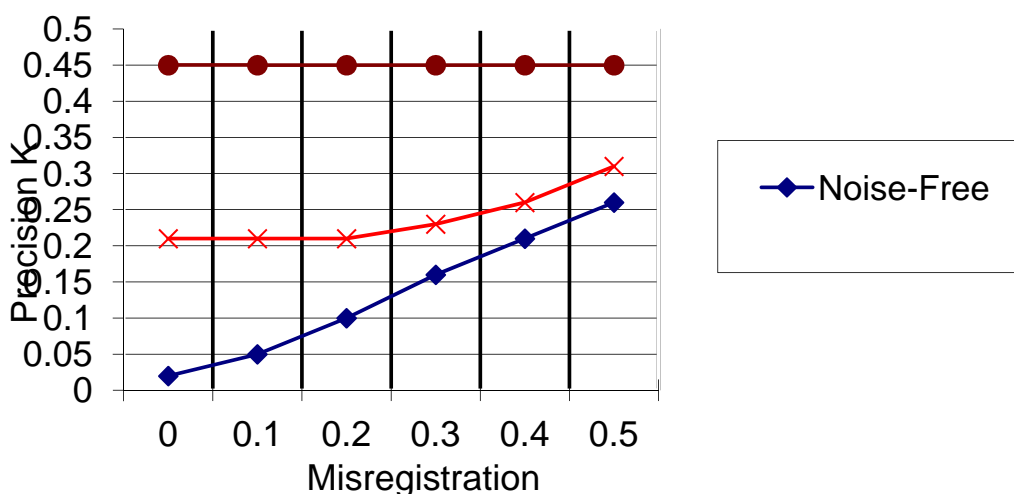


**Figure 9. Degradation of the SST precision as a function of imperfections in the Band-to-Band Registration. The misregistration ranges from 0.0 to 0.5 of the pixel area.**

#### 3.4.2.3 Modulation Transfer Function

Two 1.3-km resolution AVHRR nadir scenes were chosen as SST Modulation Transfer Function (MTF) test sites. One over the open ocean, and the other spanning the large horizontal SST gradients associated with the edge of the Gulf Stream. The VIIRS TOA radiances of all thermal bands were simulated using radiative transfer modeling. Only one atmosphere was used in each scene. The data were interpolated into 450 m resolution and a 9-point smoothing was performed to all the data to reduce noise.

Seven SBRS MTF models were applied to both scenes. The MTF models are circular Gaussian models of MTF, numbered from 1 (sharpest) to 7 (least sharp). Model 1 is 0.7 at Nyquist. Model 7 is 0.1 at Nyquist. Model 3 is 0.5 at Nyquist, (as specified for the imagery bands). Model 5 is 0.3 at Nyquist, (as specified for the moderate bands). The Ground Sampling Distances (GSDs) vary from 150 m to 1250 m. The Horizontal Cell Size (HCS) is 1.3 km.

### SST Precision vs MTF (SCENE II)

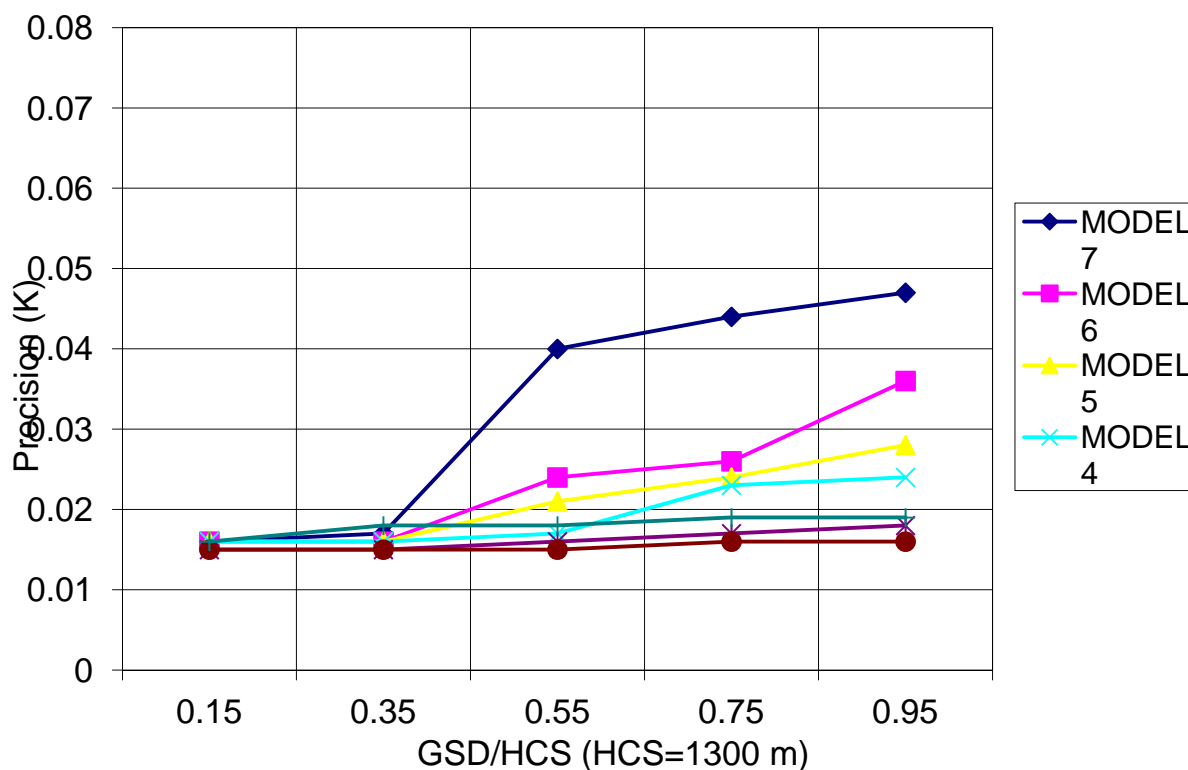


**Figure 10. Degradation of the VIIRS daytime SST retrievals for different models of the MTF, as a function of the Ground Sampling Distance. These results are from a scene containing the Gulf Stream.**

Figure 10 shows the VIIRS baseline split window algorithm MTF results from the Gulf Stream Scene. The results indicate that the MTF models do not introduce a dominant error in the SST retrievals, especially for small GSDs.

The AVHRR scenes used in this analysis were selected because of the lack of cloud. A potential post-launch problem with the actual BBR and MTF properties of the VIIRS could occur in the vicinity of the edges of very cold cloud, such as towering cumulus in the tropics, where a brightness temperature change of up to 100K can occur over a small number of pixels. If this is found to be a problem with the on-orbit data, it may be necessary to “erode” the VIIRS cloud mask to flag as possibly cloudy pixels adjacent to such cloud edges (e.g. Casey and Cornillon, 1999)

### 3.4.2.4 Combined instrumental effects

The diverse sources of instrumental effects can be calculated for a range of scene temperatures using information derived from the prelaunch calibration and characterization of the sensor. The net instrumental effect is derived by a “root sum square” of the individual components that are assumed to be uncorrelated. An example of the graphical display of this is shown in Figure 11 for the 10.8  $\mu\text{m}$  band (M15). Tables 4 and 5 give the RSS errors for the VIIRS infrared bands as a function of scene temperature.

**Table 4. VIIRS Fractional Radiance Uncertainty**

Temp (K)	VIIRS Bands			
	3.7 $\mu\text{m}$ M12	4.0 $\mu\text{m}$ M13	10.8 $\mu\text{m}$ M15	12.0 $\mu\text{m}$ M16
260	.0083	.0071	.0031	.0031
270	.0079	.0067	.0031	.0031
280	.0074	.0064	.0031	.0031
290	.007	.0061	.0031	.0031
300	.0067	.0058	.0030	.0031
310	.0064	.0055	.0030	.0030
320	.0061	.0053	.0030	.0030

**Table 5. Scene Temperature Uncertainty**

Temp (K)	VIIRS Bands			
	3.7 $\mu\text{m}$ M12	4.0 $\mu\text{m}$ M13	10.8 $\mu\text{m}$ M15	12.0 $\mu\text{m}$ M16
260	0.15	0.13	0.16	0.18
270	0.15	0.14	0.17	0.19
280	0.15	0.14	0.18	0.20
290	0.15	0.14	0.19	0.21
300	0.16	0.14	0.20	0.22
310	0.16	0.15	0.22	0.24
320	0.16	0.15	0.23	0.25



Preliminary Uncertainties for VIIRS TEB Band 11 ( $\lambda_{\text{ctr}}=10.800 \mu\text{m}$ ,  $L_{\text{deg}}=9.66$ )  
(Estimated variable uncertainties shown in parentheses)

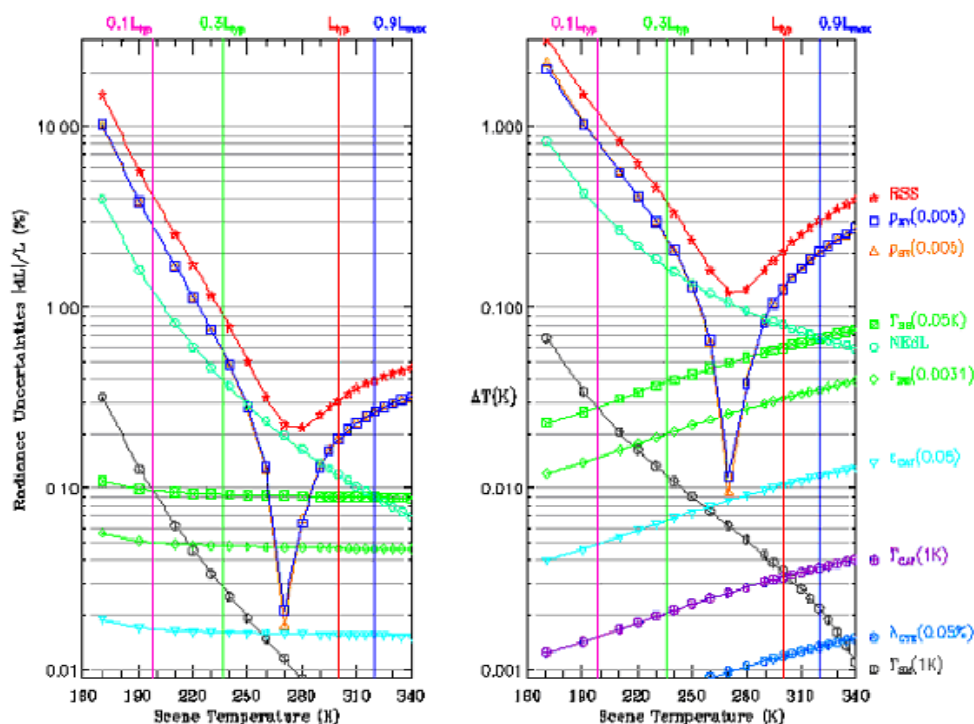


**Figure 11. Components of the instrumental sources of error in the VIIRS M15 band at 10.8  $\mu\text{m}$ . The left hand panel shows the errors as a percentage of the radiance measurement, and the right panel after conversion temperature.**

### 3.4.2.5 Parametric dependences of the SST errors

Using the synthetic data set a study of the dependences of the instrumental error sources on the derived EDRs has been conducted, in which the some aspects of the instrumental error sources we systematically modified to determine the parametric dependences of the errors in the EDRs. This produces an estimate of the sensitivity of the SST retrievals on individual sources or error. An estimate of the inherent algorithm error is also derived in this analysis, which is illustrated schematically in Figure 12.

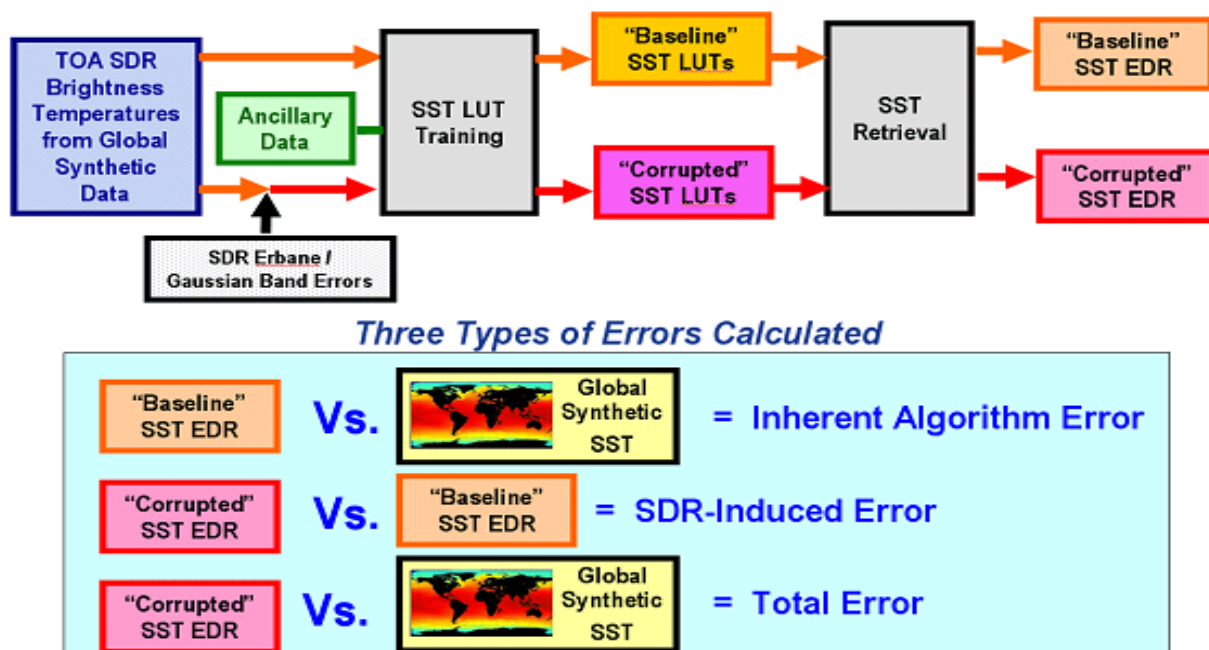


**Figure 12. Schematic flow-diagram of the SST EDR error analysis**

The inherent algorithm uncertainties are illustrated in Figure 13, for nadir measurements ( $\theta < 40^\circ$ ) and summarized in Table 6, where values for the edge of swath are also given. The "Margin" is the proportion of the target uncertainties not consumed by the uncertainties due solely to the algorithm, and therefore available for all of the uncertainties in the SDR. The margin ranges from 30% to 50%, with most being available at nadir at night, when there infrared bands are used for the atmospheric correction.

**Table 6. Global SST uncertainties cause by inherent algorithm error.**

Daytime			Nighttime		Day & night	
Target K	Uncertainty K	Margin	Uncertainty  K	Margin %	Uncertainty K	Margin %
Nadir						
0.4	0.302	35	0.193	52	0.253	37
Edge of Swath						
0.7	0.475	32	0.350	50	0.418	40

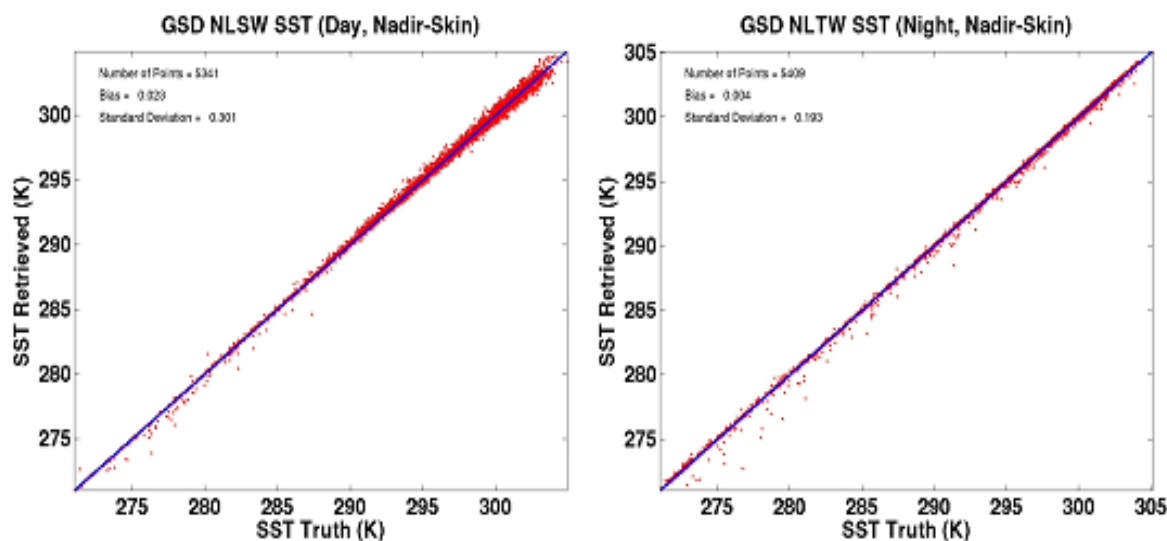


**Figure 13. Scatter diagrams of the simulated skin SST retrievals, for the daytime NLSW algorithm at left, and the night-time triple band algorithm at left. The daytime retrievals display increasing scatter at higher SSTs, related to associated with increased atmospheric water vapor concentrations.**

Figure 14 displays the dependences of the skin SST errors on uncorrelated noise in each of the infrared band, and indicates a more pronounced increased in uncertainty in the daytime, two-channel retrievals at higher SST, which reflects the higher atmospheric water-vapor content. This is consistent with the experience with MODIS SST retrievals, where the nighttime SST measurements are derived using a split-window algorithm using two narrow bands in the mid-infrared atmospheric window are demonstrably more accurate than the retrievals based on a split-window algorithms in the thermal infrared atmospheric transmission window.

Using the Global Synthetic Data set, the sensitivity of the SST retrievals on SDR errors has been determined through a parametric analysis in which the synthetic brightness temperatures have been subjected to increasing levels of noise and bias errors. The results of the addition of random noise, uncorrelated between the different bands, are summarized in Figure 14, where the independent variable is the SDR error given as a percentage of the brightness temperature measurement. The left column are the results of the simulations in the nadir section of the swath ( $\theta < 40^\circ$ ) and the right column for the end of swath ( $40^\circ < \theta < 53^\circ$ ). The target accuracy is shown in all panels by the yellow line. The top row shows the effects of the random noise in the SDR alone in the daytime (blue), night-time (green), and for combined day-and-night retrievals (pink). The panels in the center row show the SDR error contribution for the day-and-night simulations, (taken from the top panels) and the total SST errors for the day-and-night combination including the inherent algorithm error. The bottom panels show the total skin SST errors, separately for the day and night simulations as well as the day-and-night combination. The daytime errors are somewhat more sensitive to contributions to errors from band M15 ( $\lambda=10.8 \mu\text{m}$ ) than in band

M16 ( $\lambda=12.0\ \mu\text{m}$ ), as more weight is attached in the atmospheric correction algorithm to the M12 measurements, where the atmosphere is more transparent. The night-time skin SST errors do not appear to be more sensitive to SDR errors in any one of the individual three bands.

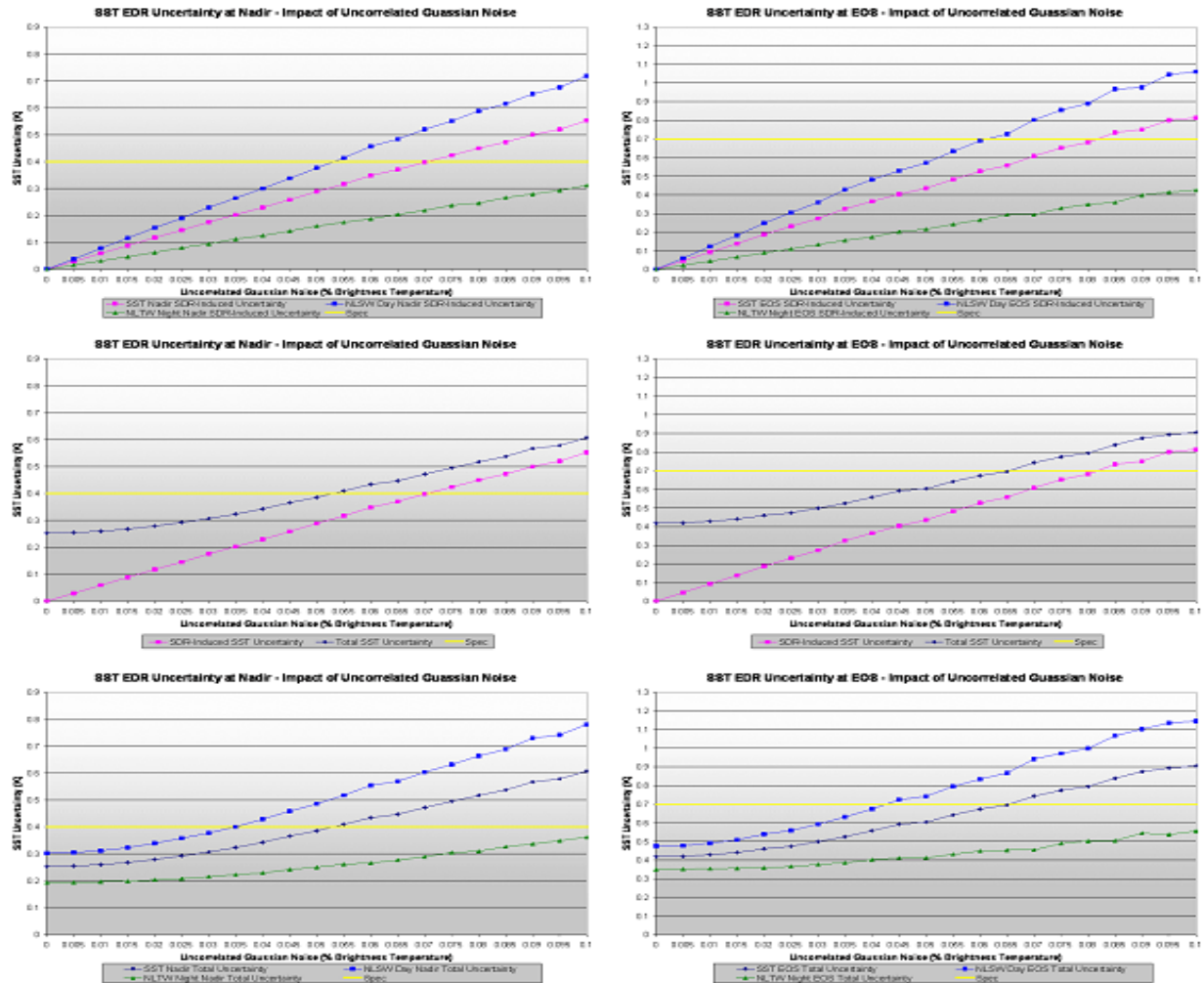


**Figure 14.** Dependences of the skin SST errors on uncorrelated noise in each of the infrared band, expressed as a percentage of the brightness temperature. The top panel shows the SDR errors for the night-time algorithm (green), daytime algorithm (blue) and the day-and-night combination (pink). The center panels show the SDR errors (day-and-night; pink line) and the total error that includes the contribution of the inherent algorithm error (dark blue). The bottom panels show the total skin SST errors for the day-and-night combination and separately for the retrievals during daytime (blue) and nighttime (green). The left column are the results of the simulations in the nadir section of the swath ( $\theta < 40^\circ$ ) and the right column for the end of swath ( $40^\circ < \theta < 53^\circ$ ). The target accuracy is shown in all panels by the yellow line.

These results demonstrate that the night-time triple band algorithm is more robust to SDR errors than the daytime, split-window retrievals. The error budget remains within the target accuracy

for all values of the SDR errors up to 0.1% for the nighttime retrievals, whereas during the day, the target accuracy is met only for much smaller errors in the SDR measurements.

The other type of contributions to the SST error budget arises from systematic bias errors in the SDRs. These could be caused by errors in the calibration procedure, such as in the temperature of the black body target which could affect all infrared bands in a correlated fashion; stray light or cross-talk (including “ghosting”) in the optical path of the instrument which could influence some bands, or even just some detectors, and not others; or imperfections in the knowledge of the angular and spectral properties of the reflectivity of the Half-Angle Mirror, which would introduce correlated bias errors in the different bands. Whether the HAM-induced errors are correlated or anti-correlated will depend on the differences between the mirror reflectivity model built into the processing stream, and the actual properties of the HAM. To investigate the consequences of SDR bias errors on the SST retrievals, the SDR radiances were systematically adjusted, by up to 3%, and the consequences quantified. The radiances were adjusted in M12, M15 and M16, in both correlated and anti-correlated fashions, leading to eight sets of numerical experiments for the nighttime algorithm, and four for the daytime algorithm.

Given that it is planned to derive the coefficients for the atmospheric correction algorithms from matchups with surface data, the systematic bias errors will be corrected in the sense of minimized global rms errors; i.e. the SDR bias errors are treated as part of the atmospheric effect. The threshold value in the brightness temperature differences between the two stratifications in the daytime NLSW SST algorithm is sensitive to bias errors and it was found that anti-correlated SDR errors larger than  $\sim 0.8\%$  of the radiance measurement between bands M15 and M16, require the switch point to be recalculated. Experience with MODIS has shown that the SST algorithm coefficients have to be recalculated on a monthly basis to account for seasonal effects in the atmosphere; this approach also compensates for seasonally varying artifacts from the instrument that might be caused by changing solar illumination of the spacecraft.

The relative immunity of the derived SST fields to systematic bias errors in the SDRs is only conferred once robust coefficients have been derived from a large matchup data base. Prior to this, when the coefficients used in the SST retrieval are those derived from pre-launch simulations, then unanticipated, and therefore uncorrected, instrumental artifacts may result in bias errors, perhaps significant ones, in the derived SSTs.

## **3.5 PRACTICAL CONSIDERATIONS**

### **3.5.1 Numerical Computation Consideration**

In order to retrieve SST within an operational processing environment, statistical algorithms that meet quality requirements have been developed that are much quicker than physical modeling methods. Pre-generated LUTs are used to speed processing yet retain flexibility. This approach has been successfully demonstrated with the MODIS SST retrievals. The revision of the values of LUTs to account for new knowledge of the instrument behavior, including time-dependent degradation of the instrument performance, and new, possibly time dependent, coefficients for the atmospheric correction algorithms, is much easier to achieve than revisions to the computer

code. However, some improvements in our understanding of the instrument characteristics, and how to compensate for unanticipated artifacts may still require modifications to the code.

### 3.5.2 Programming and Procedural Considerations

The simplicity of all the algorithms described in this document translates into very small amounts of code using basic mathematical routines. Computationally intensive processes are performed offline, with results delivered as re-generated LUTs.

### 3.5.3 Configuration of Retrievals

Adjustable parameters for the retrieval of the SST products allow selection of atmospheric classifications, separate selection of retrieval algorithms for skin SST and for bulk SST. The flexibility built into the architecture also allows easy implementation of possible future developments.

### 3.5.4 Quality Assessment and Diagnostics

A number of parameters and indicators are reported in the SST product as retrieval diagnostic flags. Statistical information is reviewed for quality assessment. Table 7 lists the available quality flags. The final list of delivered flags will be determined in the operational environment.

**Table 7. VIIRS SST EDR Quality Flags**

Byte	VIIRS SST Flag	Result	Bits
0	Skin SST quality	11 = High Quality 10 = Degraded 01 = Excluded 00 = Not retrieved	2

Byte	VIIRS SST Flag	Result	Bits
	Bulk SST quality	11 = High Quality 10 = Degraded 01 = Excluded 00 = Not retrieved	2
	SST State	10 = Average 01 = Moist 00 = Dry / None	2
	Algorithm	1 = Triple Window 0 = Non-linear Split Window	1
	Day / Night	1 = Day 0 = Night	1
1	Bad LWIR SDR	1 = Bad SDR 0 = Good SDR	1
	Bad SWIR SDR	1 = Bad SDR 0 = Good SDR	1
	Cloud Confidence	11 = Confident Cloudy 10 = Probably Cloudy 01 = Probably Clear 00 = Confident Clear	2
	Adjacent Pixel Cloud Confident Value	11 = Confident Cloudy 10 = Probably Cloudy 01 = Probably Clear 00 = Confident Clear	2
	Thin Cirrus	1 = Thin Cirrus 0 = No Thin Cirrus	1
	Sea Ice	1 = Sea Ice 0 = No Sea Ice	1

Byte	VIIRS SST Flag	Result	Bits
<b>2</b>	Sun Glint	1 = Sun glint 0 = No sun glint	1
	Exclusion, AOT > 1	1 = Yes 0 = No	1
	Degraded, AOT > 0.6	1 = Yes 0 = No	1
	Exclusion, Not Ocean	1 = Not ocean 0 = Ocean	1
	Degraded, HCS limit	1 = Past HCS limit 0 = Within HCS limit	1
	Degraded, Sensor Zenith Angle > 40	1 = Yes 0 = No	1
	Skin SST Outside Range	1 = Out of range 0 = In range	1
	Bulk SST Outside Range	1 = Out of range 0 = In range	1
<b>3</b>	Skin SST Degraded, T > 305 K	1 = Degraded 0 = Not degraded	1
	Bulk SST Degraded, T > 305 K	1 = Degraded 0 = Not degraded	1
	Spare Bit		1
	Spare Bit		1
	Spare Bit		1
	Spare Bit		1
	Spare Bit		1
	Spare Bit		1

### 3.5.5 Exception Handling

Pixels identified by the cloud mask as confident cloudy are not processed.



## 3.6 ALGORITHM VALIDATION

### 3.6.1 Pre-Launch Validation

The atmospheric correction algorithm will be derived pre-launch by radiative transfer modeling to simulate the VIIRS TIR channel measurements. Selected radiosondes from the operational network stations or field campaigns will be used in the VIIRS simulations for the development of the atmospheric correction algorithm. Measurements from the operational surface drifting and fixed buoy programs will be used to characterize the surface temperature fields and to validate the atmospheric correction algorithms. The assimilated meteorological fields provided by NCEP and ECMWF provide a valuable description of the marine atmosphere and surface temperature. These fields will be used in conjunction with the radiative transfer modeling to simulate the VIIRS measurements in order to validate the radiosonde data and to provide direct input to the radiative transfer modeling process.

Measurements from AVHRR and ATSR will be used in the pre-launch phase to study the error characteristics of the SST retrieval.

To date, the accuracy, precision, and uncertainty requirements for this EDR are for retrieval of skin SST. However, both skin SST and bulk SST can be retrieved using the same algorithm forms. Currently, the baseline VIIRS algorithm is a dual split window retrieval using two MWIR bands and two LWIR bands. When sun glint prevents the use of the MWIR bands, the software architecture is designed to fall back to the LWIR split window algorithm. Pre-launch, the coefficients for skin retrieval will be derived from *in situ* radiometric measurements and from other physical retrievals such as ATSR. The coefficients for bulk retrieval will be derived from buoy and other bulk measurements, and from retrievals such as AVHRR.

### 3.6.2 Post-Launch Calibration and Validation

As with the heritage sensors, the post-launch monitoring of the characteristics of the VIIRS instrument, and in particular the quantitative radiometry of the infrared bands, can only be done using the internal calibration procedures and the instrument “housekeeping” measurements. Failure to account for the inevitable on-orbit degradation of the instrument and will lead to a progressive increase in the errors of the SST retrievals. Again, building on the experience gathered with the heritage sensors, comparisons with coincident *in situ* measurements of the SST so that the time evolution of the error characteristics of the VIIRS SST can be determined throughout the lifetime of the instruments. Where feasible, the same measurements will be used to derive updates and corrections to the processing algorithms to compensate for the instrument ageing.

It will be necessary to establish global or at least appropriately distributed programs of SST measurements for post-launch validation and updating of coefficients. This will require a number of infrared radiometers installed on ships and, possibly, moored buoys to routinely collect skin SST measurements. The deployment on moorings will require significant instrument development. Along with these radiometric skin SSTs a range of other supporting parameters should also be measured. These include bulk SST and other parameters that influence the skin to bulk temperature differences. In addition, relevant atmospheric parameters can be derived from

VIIRS or other spacecraft instruments, such as total column atmospheric moisture measured by microwave radiometers. In determining the scope of the validation exercise, it is important to recognize that, based on experience with the heritage instruments, only about 10% of possible coincidences between the satellite and validating measurements are suitable; the remaining ~90% have to be discarded because of cloud effects in the satellite data.

Several groups have developed radiometer systems that can be installed on ships of opportunity. The locations of the instruments on their host ships, and the ships themselves, are shown in Figure 15. In each case the radiometer has to view the sea surface ahead of the disturbance of the bow wave, and to have a view of the sky for measurement of sky radiance needed for the



**Figure 15. Radiometers installed on ships for the validation of MODIS skin SSTs. Top: the ISAR mounted above the bridge of the M/V *Jingu Maru*. Middle: CIRIMS mounted above the bridge of the NOAA S *Ronald H. Brown*. Bottom: M-AERI mounted on an upper deck of the *Explorer of the Seas*.**

correction of the reflected component in the sea-viewing measurement (Figure 16). These systems operate autonomously and report by satellite, providing a real time set of skin SST measurements. These include the CIRIMS (Calibrated Infrared In Situ Measurement System; Jessup and Branch, 2008) and ISAR (Infrared Sea Surface Temperature Autonomous

Radiometer; Donlon et al., 2008) on research vessels, such as the NOAA Ship *Ronald H Brown*, the R/V *Thomas G. Thompson* and the USCGC *Polar Sea* (Jessup and Branch, 2008), and commercial ships (notably the *Jingu Maru* of NYK Lines and M/V *Pride of Bilbao* operated by P&O Ferries between the UK and Spain (Donlon et al., 2008)). A more complex instrument, the Marine-Atmospheric Emitted Radiance Interferometer (M-AERI; Minnett et al., 2001) was developed to be the main radiometric validation sensor for MODIS, and has been deployed on 45 cruises covering a wide range of conditions from the High Arctic to the coast of Antarctica. On these deployments the instruments have been accompanied by a trained operator, but on a six-year deployment on the Royal Caribbean cruise ship *Explorer of the Seas* (Williams et al., 2002), the instruments have operated essentially unattended. This has shown that even sophisticated instruments can be operated autonomously with maintenance being undertaken during port visits. The M-AERI has also been used for the validation on the AVHRR Pathfinder SST (Kearns et al., 2000), and the instruments on the *Explorer of the Seas* for the validation of the AATSR on *Envisat* (Noyes et al., 2006).

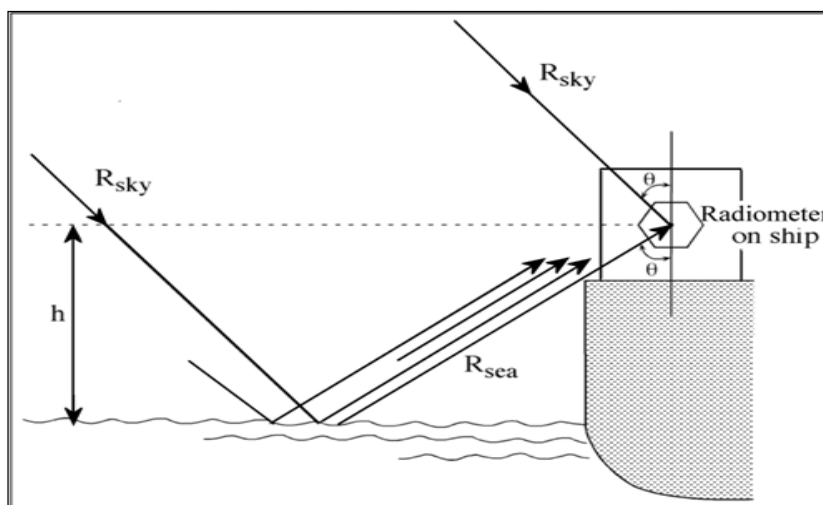


**Figure 16. The measurement geometry of a ship-mounted radiometer taking a skin SST measurement. The reflected sky radiance is corrected using a direct measurement of the sky emission, and an accurate value of the surface reflectance (equal to 1-emissivity).**

The geographical, and climatological, ranges of the measurements from these radiometers are shown in Figure 17

To ensure accuracy and consistency of the skin SST measurements from the different radiometers, a series of workshops has been held at the Rosenstiel School of the University of Miami. The first inter was held during March 1998. This involved several high quality radiometers and some off-the-shelf devices. NIST (National Institute of Standards and Technology) provided their standard black body target (Fowler, 1995) for the calibration of each radiometer. Other black body calibration targets included a NIST water-bath black-body calibration target provided by the University of Washington, a smaller unit from JPL, the CASOTS (Combined Action to Study the Ocean's Thermal Skin) black body (Donlon et al., 1999), and a portable unit designed by CSIRO, Australia. Details of the first calibration and

inter-comparison can be found at <http://www.rsmas.miami.edu/ir/>, and in an article written by Kannenberg, 1998.

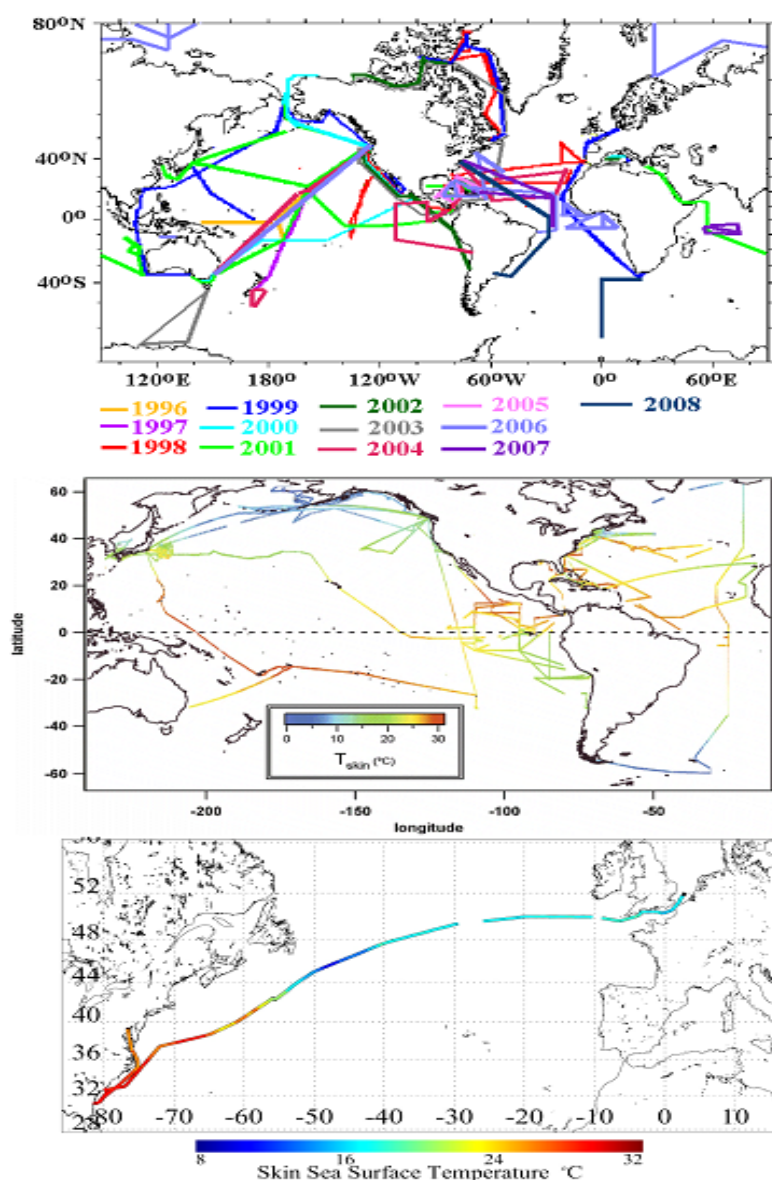


**Figure 17. Distributions of the skin SST measurements made from the M-AERI (top), and the CIRIMS (center; from Jessup and Branch, 2008). Bottom: Skin SST measurements from the ISAR on a trans-Atlantic voyage of the M/V *Jingu Maru* from US east-coast ports to Europe, 10-23 July, 2005. The color bar shows the wide range of skin SSTs measured on a single voyage.**

The second infrared workshop was held in 2001 and brought together the newly developed CIRIMS (Jessup and Branch, 2008; Branch et al., 2008) and ISAR (Donlon et al., 2008). A particularly important aspect of the Second workshop was the use of the NIST Earth Observing System Transfer Radiometer (TXR; Rice and Johnson, 1998) to characterize the laboratory black

body calibration targets used to calibrate the field-deployable radiometers (Rice et al., 2004). To compare the performance of the radiometers in realistic conditions of a field deployment, the instruments were mounted on the R/V *Walton Smith* for a short cruise out of Miami (Barton et al., 2004). The results of the Workshop included a characterization of the laboratory calibration targets used in a range of institutes, and a quantification of the uncertainties in the radiometer measurements of skin SST that contribute to the error budget of the satellite SST validation. The workshop results were published in the refereed literature (Rice et al., 2004; Barton et al., 2004).

A third workshop is being planned for the first half of 2009 under the auspices of the Committee on Earth Observation Satellites (CEOS<sup>1</sup>). It is a requirement that similar workshops be held in the NPOESS era. Otherwise, unknown discrepancies between the skin SSTs derived from different validating radiometers will be make unnecessary contributions to the VIIRS error budget. Investment in the existing radiometers and in next-generation designs is required to ensure that this resource will be available and of the necessary accuracy for VIIRS validation.

Although surface based radiometers provide the most appropriate measurements with which to validate the VIIRS skin SSTs, they are relatively small in number. The philosophy adopted for the MODIS SST validation offers a way of enhancing these data sets through the use of near-surface bulk temperatures from drifting and moored buoys, with a simple correction for the thermal skin effect. The spatial coverage of the buoys is presently extensive, but not perfect. Some areas are poorly sampled even with the drifting buoys (Figure 18). The enhancement of the distribution of the buoys during the VIIRS missions by additional drifters should be considered as a necessary component of the VIIRS SST validation.

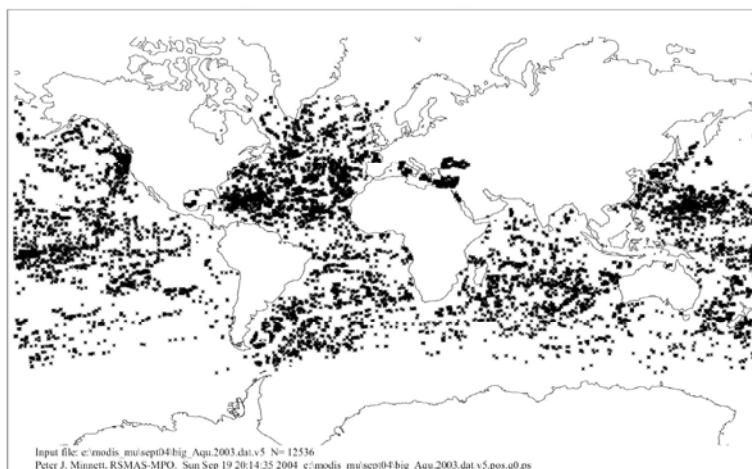


**Figure 18. The distribution of the matchups between the MODIS on Aqua and bulk SST measurements from drifting and moored buoys, for 2003. There are 12,536 matchups with the highest quality flag (QF=0)**

<sup>1</sup> <http://calvalportal.ceos.org/CalValPortal/welcome.do>



In recent years over 3000 profiling buoys have been deployed throughout the oceans in the ARGO program (Figure 19; and see <http://www.argo.ucsd.edu/>). The presently-deployed profilers measure pressure, conductivity and temperature (from which ocean salinity and density can be calculated). The profilers drift at depth and at intervals of about ten days rise to the surface, taking measurements as they ascend, and then transmit their data via satellite telemetry. The sensors however, do not measure in the uppermost ten meters or so of the water column and so are not ideal for satellite skin SST retrievals. However, a second generation of profiles is being considered that would take measurement up to the surface, and these might be suitable to contribute to VIIRS SST validation effort. With approximately 300 floats breaking surface each day, about 50 can be expected to be reporting their measurements within an hour of the satellite overpass (both night and day), of which perhaps five would be in sufficiently cloud-free conditions for the measurements to be useful for VIIRS validation.

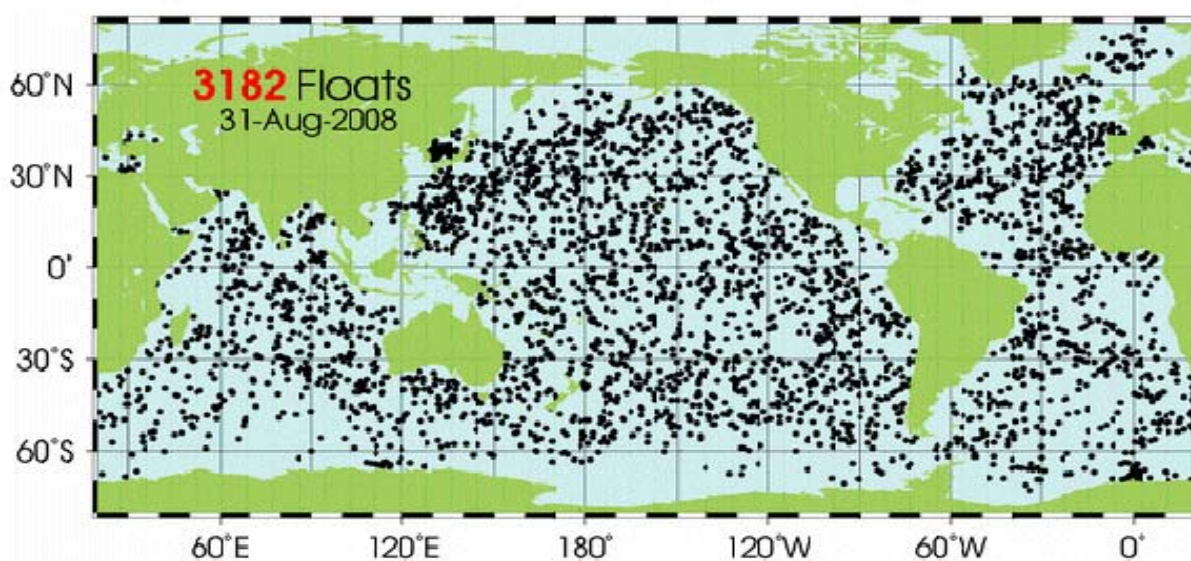


**Figure 19. Distribution of ARGO floats. From <http://www.argo.ucsd.edu/>.**

Experience has shown that all new instruments behave slightly differently than expected, making the need for *in situ* validation fundamental to the success of the VIIRS SST mission. The requirement to demonstrate the SST accuracies of the VIIRS dictate that the *in situ* measurements have higher demonstrated accuracy themselves in order to act as a reference for the satellite data

### 3.7 ALGORITHM DEVELOPMENT SCHEDULE

At the time of writing, the base-line algorithms have been tested and delivered.

## 4.0 ASSUMPTIONS AND LIMITATIONS

### 4.1 SENSOR PERFORMANCE

The VIIRS SST retrieval is feasible only under clear sky conditions; this is a limitation common to all infrared remote sensing of the surface temperatures from satellites. Another limitation on the accuracy of the SST retrievals results from the effects of increasing atmospheric path length at large scan angles. The VIIRS SST retrievals will be most accurate near the center of the swath. Note that the accuracy, precision, and uncertainty performance is specified only for the center 2000 km of the swath.

### 4.2 Derivation of Bulk SST from Skin SST

The VIIRS SST algorithms for skin and bulk SST are based on statistical regression analyses. The coefficients for the algorithms are derived using skin or bulk *in situ* measurements. Bulk SST may also be derived from skin SST, through the development of an algorithm that uses the bulk-skin temperature difference. Our current architecture supports a simple conversion scheme, and it is extensible to a more complex algorithm.

The bulk-skin temperature difference is subject to both net surface heat flux and the momentum flux (Saunders, 1967). A number of equations have been used to find the bulk-skin temperature difference (e.g., Hasse, 1971; Schluessel et al., 1990). For example, Schluessel *et al.* used following equations to calculate the skin-bulk temperature difference  $\Delta T$ :

**Nighttime:**

$$\Delta T = a_0 + a_1 u(T_s - T_a) + a_2 u(Q_s - Q_a) + a_3 L \quad (5)$$

**Daytime:**

$$\Delta T = a_0 + a_1 S / u + a_2 (Q_s - Q_a) + a_3 L \quad (6)$$

where,  $T_s$  and  $T_a$  are temperatures of surface and air,  $Q_s$  and  $Q_a$  are water vapor mixing ratios of surface and air,  $L$  is the net longwave radiative flux,  $S$  the net solar radiative flux,  $u$  the mean wind velocity, and  $a_0$ ,  $a_1$ ,  $a_2$  and  $a_3$  are coefficients that are different in each equation.

More recently, a much simpler parameterization was developed from a large set of ship-based radiometric skin SSTs measurements and coincident bulk temperatures (Donlon et al., 2002):

$$\Delta T = a_0 + a_1 \exp(a_2 * u) \quad (7)$$

where  $\Delta T$  is the skin-bulk temperature difference, and  $u$  is the true wind speed. This expression was developed from measurements at night to avoid the complexities of diurnal heating (e.g. Minnett, 2003). Comparing daytime skin SST measurements from the M-AERI (Minnett et al., 2001) with bulk SSTs from a depth of a few cm taken by a surface-following float, the same

wind speed dependence of the thermal skin effect has been found, albeit with slightly different coefficients (Minnett et al., 2008). The use of the shallow bulk SST removes nearly all of the influence of any diurnal heating from the comparison.

The simple formulation of Donlon et al. (2002) is much simpler to implement in an operational processing environment than those of Schluessel et al. (Horrocks et al., 2003). The residual scatter in the predictions of  $\Delta T$  using the Donlon et al parameterization is approximately 0.13 K, which includes a contribution from the uncertainties in the measurement of wind speed (Minnett et al., 2008).

Figure 20 shows the mean annual skin - bulk temperature difference using the Donlon et al (2002) formulation and the mean wind speed derived from over two decades of measurements from the SSM/I. (Woods et al., 2008). The wind field measurements were used to determine the parameters of Weibull distributions on monthly time scales, and these were used to derive probability functions of the thermal skin effect. The global spatial distribution of the means is encompassed by several tenths of a degree, which is much smaller than the ranges previous estimates, but which still represents a very significant contribution to the error budget of the sub-surface bulk SST retrieval.

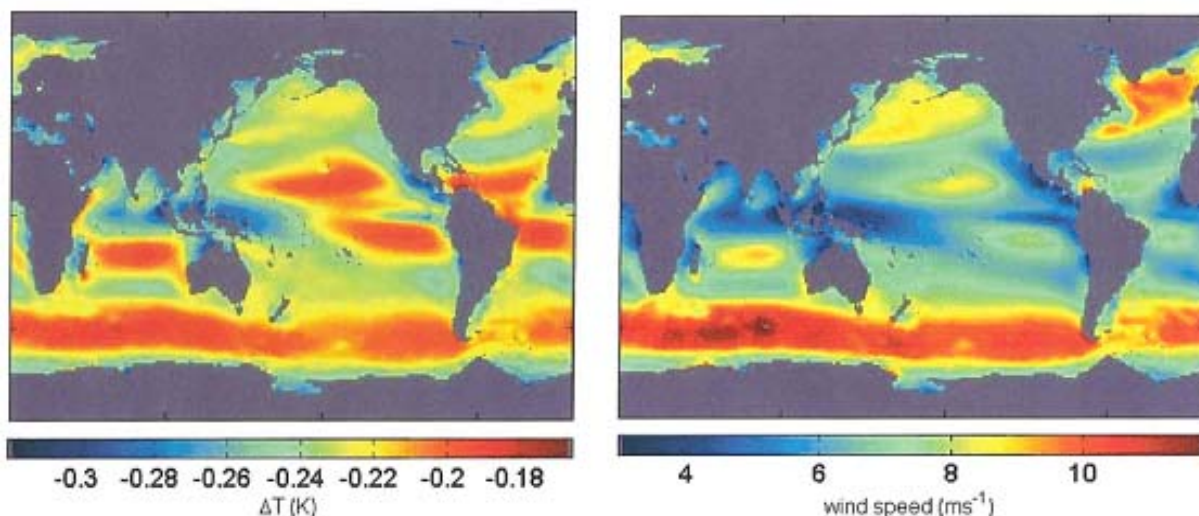


**Figure 20. Mean annual skin-bulk SST difference (left panel), and the surface wind field at the same time (right panel). From Woods et al., 2008.**

A bulk to skin conversion algorithm could be developed for the VIIRS operational environment using wind speed fields from NCEP, for example.

Another physical factor that complicates the prediction of the bulk SST from the skin SST retrieval is the diurnal thermocline. This is a vertical temperature gradient that forms in the upper several meters in conditions of low winds speed and high insolation when the solar energy input is not distributed throughout the mixed layer by wind-driven turbulent mixing. When the winds are consistently low during the day, the timing of the daily maximum in skin SST is mid-afternoon. When the winds are variable in the course of the day, the maximum value in SST is



very closely linked to the minima in winds speed (Gentemann and Minnett, 2008). The heat loss to the atmosphere during the night results in convective mixing, even in the absence of winds, that tends to eradicate the vertical temperature gradients associated with the diurnal heating. The problem that diurnal heating brings to the retrieval of bulk SSTs is that the relationship between the subsurface bulk and the skin SSTs is very time and depth dependent (e.g. Ward, 2006). Much attention has been directed to the modeling of the diurnal heating in recent years, some of which is related to producing an accurate composite SST fields from satellites with different overpass times in the GHRSSST project (Donlon et al., 2007). This work has resulted in several new models of diurnal heating and cooling (e.g. Gentemann et al., 2003; Stuart-Menteth et al., 2005a; Stuart-Menteth et al., 2005b; Gentemann et al., 2008a). Some models are being implemented in an experimental mode at NWP forecast centers. Such models, could be used to improve the accuracy of the sub-surface bulk SST retrievals from VIIRS.

### 4.3 Physical SST Retrieval

Although physical retrievals have not been used for operational SST retrieval due to the large computational requirement and possible instability, they are promising methods for improving the retrieval precision. In order to be useful in an operational setting, sufficient processing power needs to be allocated for the forward modeling (Merchant et al., 2008). Alternately, it may be possible to develop extensive LUTs for operational use, with those tables populated by offline radiative transfer modeling..

## 5.0 REFERENCES

- Barton, I. J., A. J. Prata, and D. T. Llewellyn-Jones (1993). Adv. Space Res., 69., 1993: The Along Track Scanning Radiometer – an Analysis of coincident ship and satellite measurements. *Advances in Space Research*, **13**, 69-74.[doi:10.1016/0273-1177\(93\)90529-K](#)
- Barton, I. J., P. J. Minnett, C. J. Donlon, S. J. Hook, A. T. Jessup, K. A. Maillet, and T. J. Nightingale, 2004: The Miami2001 infrared radiometer calibration and inter-comparison: 2. Ship comparisons. *Journal of Atmospheric and Oceanic Technology*, **21**, 268-283
- Berk, A., L. S. Bernstein, and D. C. Robertson, 1989: MODTRAN: A moderate resolution model for LOWTRAN 7. Spectral Sciences, Inc. Burlington, MA.
- Branch, R., A. T. Jessup, P. J. Minnett, and E. L. Key, 2008: Comparisons of Shipboard Infrared Sea Surface Skin Temperature Measurements from the CIRIMS and the M-AERI. *Journal of Atmospheric and Oceanic Technology*, **25**, 598-606.[doi: 10.1175/2007JTECHO480.1](#)
- Brown, O. B. and P. J. Minnett, 1996: MODIS Infrared Sea Surface Temperature Algorithm Algorithm Theoretical Basis Document, Version 2.0.
- Casey, K. S. and P. Cornillon, 1999: A Comparison of Satellite and In Situ-Based Sea Surface Temperature Climatologies. *Journal of Climate*, **12**, 1848-1863.
- Chen, S. S. and R. A. Houze, 1997: Diurnal variation and lifecycle of deep convective systems over the tropical Pacific warm pool. *Quarterly Journal of the Royal Meteorological Society*, **123**, 357-388
- Chesters, D., L. W. Uccellini, and W. D. Robinson, 1983: Low-level water vapor fields from the VISSR Atmospheric Sounder (VAS) "split window" channels. *Journal of Climate and Applied Meteorology*, **22**, 725-743
- Clough, S. A., F. X. Kneizys, and R. W. Davies, 1989: Line shape and the water vapor continuum. *Atmos. Res.*, **23**, 229-241
- Cornette, W. M., P. K. Acharya, D. C. Robertson, and G. P. Anderson, 1994: Moderate spectral atmospheric radiance and transmittance code (MOSART). Photon Research Associates, Inc. La Jolla, CA.
- Donlon, C., I. S. Robinson, M. Reynolds, W. Wimmer, G. Fisher, R. Edwards, and T. J. Nightingale, 2008: An Infrared Sea Surface Temperature Autonomous Radiometer (ISAR) for Deployment aboard Volunteer Observing Ships (VOS). *Journal of Atmospheric and Oceanic Technology*, **25**, 93-113
- Donlon, C., I. Robinson, K. S. Casey, J. Vazquez-Cuervo, E. Armstrong, O. Arino, C. Gentemann, D. May, P. LeBorgne, J. Piollé, I. Barton, H. Beggs, D. J. S. Poulter, C. J. Merchant, A. Bingham, S. Heinz, A. Harris, G. Wick, B. Emery, P. Minnett, R. Evans, D. Llewellyn-Jones, C. Mutlow, R. W. Reynolds, H. Kawamura, and N. Rayner, 2007: The Global Ocean Data Assimilation Experiment High-resolution Sea Surface Temperature Pilot Project. *Bulletin of the American Meteorological Society*, **88**, 1197-1213
- Donlon, C. J., T. Nightingale, L. Fiedler, G. Fisher, D. Baldwin, and I. S. Robinson, 1999: The Calibration and Intercalibration of Sea-Going Infrared Radiometer Systems Using a Low Cost Blackbody Cavity. *Journal of Atmospheric and Oceanic Technology*, **16**, 1183–1197

- Donlon, C. J., P. J. Minnett, C. Gentemann, T. J. Nightingale, I. J. Barton, B. Ward, and J. Murray, 2002: Toward improved validation of satellite sea surface skin temperature measurements for climate research. *Journal of Climate*, **15**, 353-369
- Emery, W., Y. Yu, G. Wick, P. Schluessel, and R. W. Reynolds, 1994: Correcting infrared satellite estimates of sea surface temperature for atmospheric water vapor attenuation. *J. Geophys. Res.*, **99**, 5219-5236
- Fowler, J. B., 1995: A third generation water bath based blackbody source. *J. Res. Natl.Inst. Stand. Technol.*, **100**, 591-599
- Gentemann, C. L. and P. J. Minnett, 2008: Radiometric measurements of ocean surface thermal variability. *Journal of Geophysical Research*, **113**, C08017.doi:10.1029/2007JC004540
- Gentemann, C. L., P. J. Minnett, and B. Ward, 2008a: Profiles of Ocean Surface Heating (POSH): a new model of upper ocean diurnal thermal variability. *Journal of Geophysical Research*, In review
- Gentemann, C. L., C. J. Donlon, A. Stuart-Menteth, and F. J. Wentz, 2003: Diurnal signals in satellite sea surface temperature measurements. *Geophysical Research Letters*, **30**, 1140-1143
- Gentemann, C. L., P. J. Minnett, P. LeBorgne, and C. J. Merchant, 2008b: Multi-satellite measurements of large diurnal warming events. *Geophysical Research Letters*, In the press.doi:10.1029/2008GL035730
- Good, S. A., G. K. Corlett, J. J. Remedios, E. J. Noyes, and D. T. Llewellyn-Jones, 2007: The Global Trend in Sea Surface Temperature from 20 Years of Advanced Very High Resolution Radiometer Data. *Journal of Climate*, **20**, 1255-1264.doi: 10.1175/JCLI4049.1
- Han, Y., J. A. Shaw, J. H. Churnside, P. D. Brown, and S. A. Clough, 1997: Infrared spectral radiance measurements in the tropical Pacific atmosphere. *Journal of Geophysical Research*, **102**, 4353-4356
- Hanafin, J. A. and P. J. Minnett, 2005: Infrared-emissivity measurements of a wind-roughened sea surface. *Applied Optics.*, **44**, 398-411
- Hasse, L., 1971: The sea surface temperature deviation and the heat flow at the sea-air interface. *Boundary-Layer Meteorology*, **1**, 368-379
- Horrocks, L. A., B. Candy, T. J. Nightingale, R. W. Saunders, A. O'Carroll, and A. R. Harris, 2003: Parameterizations of the ocean skin effect and implications for satellite-based measurement of sea-surface temperature. *Journal of Geophysical Research*, **108**, 3096
- Jessup, A. T. and R. Branch, 2008: Integrated Ocean Skin and Bulk Temperature Measurements Using the Calibrated Infrared In Situ Measurement System (CIRIMS) and Through-Hull Ports. *Journal of Atmospheric and Oceanic Technology*, **25**, 579-597.DOI: 10.1175/2007JTECHO479.1
- Kalnay, E., M. Kanamitsu, R. Kistler, W. Collins, D. Deaven, L. Gandin, M. Iredell, S. Sha, G. White, J. Woollen, Y. Zhu, M. Chelliah, W. Ebisuzaki, W. Higgins, J. Janowiak, K. C. Mo, C. Ropelewski, J. Wang, A. Leetmaa, R. Reynolds, R. Jenne, and D. Joseph, 1996: The NCEP/NCAR 40-Year Reanalysis Project. *Bulletin of the American Meteorological Society*, **77**, 437-471
- Kannenberg, R., 1998: IR instrument comparison workshop at the Rosenstiel School of Marine and Atmospheric Science (RSMAS). *The Earth Observer*, **10**, 51-54
- Kearns, E. J., J. A. Hanafin, R. H. Evans, P. J. Minnett, and O. B. Brown, 2000: An independent assessment of Pathfinder AVHRR sea surface temperature accuracy using the Marine-

- Atmosphere Emitted Radiance Interferometer (M-AERI). *Bulletin of the American Meteorological Society*, **81**, 1525-1536
- Kilpatrick, K. A., G. P. Podestá, and R. H. Evans, 2001: Overview of the NOAA/NASA Pathfinder algorithm for Sea Surface Temperature and associated Matchup Database. *Journal of Geophysical Research*, **106**, 9179-9198
- Kneizys, F. X., E. P. Shettle, L. W. Abreu, J. H. Chetwynd, G. P. Anderson, W. O. Gallery, J. E. A. Selby, and S. A. Clough, 1988: Users Guide to LOWTRAN 7. Air Force Geophysics Laboratory Bedford, MA.
- Legeckis, R. and T. Zhu, 1997: Sea surface temperature from the GEOS-8 geostationary satellite. *Bull. Amer. Meteor. Soc.*, **78**, 1971-1983
- Masuda, K., T. Takashima, and Y. Takayama, 1988: Emissivity of pure and sea waters for the model sea surface in the infrared window region. *Rem. Sens. of Environment*, **24**, 313-329
- May, D. A., M. M. Parmeter, D. S. Olszewski, and B. D. McKenzie, 1998: Operational processing of satellite sea surface temperature retrievals at the Naval Oceanographic Office. *Bulletin of the American Meteorological Society*, **79**, 397-407
- McClain, E. P., W. G. Pichel, C. C. Walton, Z. Ahmad, and J. Sutton, 1983: Multi-channel improvements satellite derived global sea surface temperatures. *Adv. Space Res.*, **2**, 43-47
- McMillin, L., 1975: Estimation of sea-surface temperatures from two infrared window measurements with different absorption. *J. Geophys. Research*, **80**, 5113-5117
- Merchant, C. J., A. R. Harris, J. Murray, and A. M. Zavody, 1999: Toward the elimination of bias in satellite retrievals of skin sea surface temperature. 1: Theory. modelling and inter-algorithm comparison. *J. Geophys. Res.*, **104**, 23565-23578
- Merchant, C. J., P. LeBorgne, A. Marsouin, and H. Roquet, 2008: Optimal estimation of sea surface temperature from split-window observations. *Remote Sensing of Environment*, **112**, 2469-2484
- Minnett, P. J., 2003: Radiometric measurements of the sea-surface skin temperature - the competing roles of the diurnal thermocline and the cool skin. *International Journal of Remote Sensing*, **24**, 5033-5047
- Minnett, P. J., M. Smith, and B. Ward, 2008: Measurements of the oceanic thermal skin effect. *Deep Sea Research II*, **Submitted**
- Minnett, P. J., R. O. Knuteson, F. A. Best, B. J. Osborne, J. A. Hanafin, and O. B. Brown, 2001: The Marine-Atmospheric Emitted Radiance Interferometer (M-AERI), a high-accuracy, sea-going infrared spectroradiometer. *Journal of Atmospheric and Oceanic Technology*, **18**, 994-1013
- Mutlow, C. T., D. T. Llewellyn-Jones, A. M. Závody, and I. J. Barton, 1994: Sea-surface temperature measurements by the Along-Track Scanning Radiometer (ATSR) on ESA's ERS-1 Satellite - Early results. *J. Geophys. Res.*, **22**, 575-22,588
- Nalli, N. R., P. J. Minnett, and P. van Delst, 2008a: Emissivity and reflection model for calculating unpolarized isotropic water surface-leaving radiance in the infrared. I: Theoretical development and calculations. *Applied Optics*, **47**, 3701-3721. doi:10.1364/AO.47.003701
- Nalli, N. R., P. J. Minnett, E. Maddy, W. W. McMillan, and M. D. Goldberg, 2008b: Emissivity and reflection model for calculating unpolarized isotropic water surface-leaving radiance in the infrared. 2: Validation using Fourier transform spectrometers. *Applied Optics*, **47**, 4649-4671. doi:10.1364/AO.47.004649

- Noyes, E. J., P. J. Minnett, J. J. Remedios, G. K. Corlett, S. A. Good, and D. T. Llewellyn-Jones, 2006: The Accuracy of the AATSR Sea Surface Temperatures in the Caribbean. *Remote Sensing of Environment*, **101**, 38-51
- Rice, J. P. and B. C. Johnson, 1998: The NIST EOS Thermal-Infrared Transfer Radiometer. *Metrologia*, **35**, 505-509
- Rice, J. P., J. J. Butler, B. C. Johnson, P. J. Minnett, K. A. Maillet, T. J. Nightingale, S. J. Hook, A. Abtahi, C. J. Donlon, and I. J. Barton, 2004: The Miami2001 Infrared Radiometer Calibration and Intercomparison: 1. Laboratory Characterization of Blackbody Targets. *J. Atm. Ocean. Tech.*, **21**, 258-267
- Saunders, P. M., 1967: The temperature at the ocean-air interface. *J. Atmos. Sci.*, **24**, 269-274
- Schluessel, P., W. J. Emery, H. Grassl, and T. Mammen, 1990: On the bulk-skin temperature difference and its impact on satellite remote sensing of sea surface temperatures. *Journal of Geophysical Research*, **95**, 13,341-13,356
- Smith, A. H., R. W. Saunders, and A. M. Závody, 1994: The validation of ATSR using aircraft radiometer data over the Tropical Atlantic. *J. Atmos. and Oceanogr. Techn.*, **11**, 789-800
- Sobrino, J. A., J. E. Kharraz, and Z.-L. Li, 2003: Surface temperature and water vapour retrieval from MODIS data *International Journal of Remote Sensing*, **24**, 5161-5182. doi: 10.1080/0143116031000102502
- Soloviev, A. V. and P. Schlüssel, 1994: Parameterization of the cool skin of the ocean and of the air-ocean gas transfer on the basis of modeling surface renewal. *J. Phys. Oceanogr*, **24**, 1339-1346.
- Soloviev, A. V. and P. Schlüssel, 1996: Evolution of cool skin and direct air-sea gas transfer coefficient during daytime. *Bound.-Layer Meteor.*, **77**, 45-68
- Stephens, G. L., 1990: On the relationship between water vapor over the oceans and sea surface temperature. *Journal of Climate*, **3**, 634-645
- Stuart-Menteth, A., I. S. Robinson, and P. G. Challenor, 2003: A global study of diurnal warming using satellite-derived sea surface temperature. *J. Geophys. Res.*, **108**, 3155
- Stuart-Menteth, A. C., I. S. Robinson, and C. J. Donlon, 2005a: Sensitivity of the diurnal warm layer to meteorological fluctuations. Part 2: A new parameterisation for diurnal warming. *Journal of Atmospheric and Ocean Science*, **10**, 209-234
- Stuart-Menteth, A. C., I. S. Robinson, R. A. Wellner, and C. J. Donlon, 2005b: Sensitivity of the diurnal warm layer to meteorological fluctuations part 1: observations. *Journal of Atmospheric and Ocean Science*, **10**, 193-208
- Walton, C. C., 1988: Nonlinear multichannel algorithms for estimating sea surface temperature with AVHRR satellite data. *Journal of Applied Meteorology*, **27**, 115-124
- Walton, C. C., W. G. Pichel, J. F. Sapper, and D. A. May, 1998: The development and operational application of nonlinear algorithms for the measurement of sea surface temperatures with the NOAA polar-orbiting environmental satellites. *Journal of Geophysical Research*, **103**, 27,999-28,012
- Ward, B., 2006: Near-Surface Ocean Temperature. *Journal of Geophysical Research*, **111**, C02005
- Watts, P., M. Allen, and T. Nightingale, 1996: Sea surface emission and reflection for radiometric measurements made with the along-track scanning radiometer. *Journal of Atmospheric and Ocean Technology*, **13**, 126-141
- Webster, P. J., C. A. Clayson, and J. A. Curry, 1996: Clouds, radiation, and the diurnal cycle of sea surface temperature in the tropical western Pacific. *Journal of Climate*, **9**, 1712-1730

- Williams, E., E. Prager, and D. Wilson, 2002: Research Combines with Public Outreach on a Cruise Ship. *EOS*, **83**, 590, 596.
- Woods, S., P. J. Minnett, and C. L. Gentemann, 2008: Influence of the cool skin layer on global air-sea CO<sub>2</sub> flux estimates. *In preparation*
- Wu, X. and W. L. Smith, 1997: Emissivity of rough sea surface for 8-13  $\mu\text{m}$ : modeling and verification. *Applied Optics*, **36**, 2609-2619
- Závody, A. M., C. T. Mutlow, and D. T. Llewellyn-Jones, 1995: A radiative transfer model for sea-surface temperature retrieval for the Along Track Scanning Radiometer. *J. Geophys. Res.*, **100**, 937-952